High temperature fatigue of carbon/polyimide 8-harness satin woven composites. Part II: Environmental effects

Federico Foti, Yannick Pannier, Marco Gigliotti

Version of Record: https://www.sciencedirect.com/science/article/pii/S0263822319342205
Manuscript_2a6b8b9abfc07c19f7b6df329648cb5f

High Temperature Fatigue of Carbon/Polyimide 8-harness Satin Woven Composites. Part II: Environmental Effects

Federico Foti, Yannick Pannier, Marco Gigliotti*,

Institut Pprime, CNRS, ISAE-ENSMA (Department of Physics and Mechanics of Materials), Université de Poitiers

1, Avénue Clément Ader F-86962 Futuroscope Chasseneuil, France

*marco.gigliotti@ensma.fr,

Keywords: Organic Matrix Composites (OMC), Woven Composite, High Temperature Fatigue, Environmental effect, Thermo-oxidation

Abstract

This paper focuses on high temperature fatigue of Carbon/polyimide 8-harness satin woven composite materials. Traction-traction (R=0.1) fatigue tests at 250°C are carried out on Carbon/polyimide $[45]_6$ 8-harness satin woven composites under three different environments (air, 2 bar N_2, 2 bar O_2). Part II is specifically devoted to the study of the environmental effects occurring during high temperature fatigue: strain, mechanical properties and damage evolution are characterized by Digital Image Correlation (DIC) and μ-Computed Tomography (μCT) techniques. The rich characterisation of damage extent and orientation can be naturally integrated within the context of a damage-dependent behaviour models. ~~The rich characterisation of damage extent and orientation can be provided allows damage being formalised in a way that can be naturally integrated within the context of damage dependent behaviour models~~ The effect of the environment is assessed through a description of thermo-oxidation phenomena occurring at high temperatures.

1 – Introduction

The use of Organic Matrix Composites (OMC) in the aeronautical field has significantly increased due to their high specific properties and fatigue resistance in the fibre direction. These materials are employed to replace metallic materials in producing aeronautical "cold" parts like flaps, fuselage. The employment of a new generation of textile OMC is foreseen for the realization of "warm" (150°C<T<300°C) components like nacelles, fan case or either first compressor stages. During their life, these components will be exposed to high temperature in presence of oxygen and will be loaded by mechanical loads such as tensile loads, fatigue. In these work conditions, an oxidizing environment promotes an acceleration of the fatigue degradation of the composite.

The available state of the art concerning fatigue of textile OMC focuses mainly on room temperature fatigue, with some insights about the damage mechanisms developing during fatigue and affecting the durability of such materials.

For woven based laminates, transverse cracks onset on the sample edges, as result of the coalescence of initial micro-debonding on the fibre/matrix interface ([1], [2]) and propagate in the transversal plies eventually leading to interlaminar delamination between adjacent layers ([3], [4]), splitting ([5]) related to parasite bending in weft (transverse) tows ([6]). Similar mechanisms take place in satin woven laminates [7]. Four damage stages can be identified: onset of matrix cracks in the transverse tows where the local bending-induced tensile stress reaches its maximum [8], then cracks propagation along resin rich regions ([9]). In [9] it is noted that cracks onset firstly where the bending is constrained, consequently a surface tow, more free to deform in the out-of-plane direction, will crack ever after an inner tow. Additional mechanisms for more complex textile architectures are described in [10]-[12]. Generally speaking, extensive delaminated area lead to longitudinal and transversal sliding between warp and weft tows leading to an important evolution of the longitudinal strain. The failure of the sample is related to the delamination increasing and the damage localization in a specific region and generally it consists in a relative slide of the warp and weft tows in absence of broken fibres.

There is a consistent literature concerning the fatigue behaviour of woven composites ([2], [8]) with the use of DIC (see for instance [13]-[15]) and μCT (see for instance [16]-[18]) for monitoring of damage and degradation phenomena: for satin woven composites under traction-traction fatigue load these studies show that four degradation stages can be identified (see reference [8] for comprehensive review): onset of matrix cracks in the transverse tows subjected to high local bending-induced tensile stress, crack propagation along resin rich regions or towards the longitudinal tow of the same woven ply bringing to meta-delamination, transverse crack propagation and longitudinal tow failure respectively.

Few works are available concerning high-temperature fatigue of textile composites ([19]), while the interaction between fatigue and environmental degradation of has been poorly explored: previous work on environmental fatigue of composite laminates ([20], [21]) has showed that the effect of thermo-oxidation phenomena occurring at high temperature may severely affect fatigue degradation of such materials.

In reference [21], the evolution of transverse cracks density in 90° plies in [0/90]s composite laminates during fatigue in air and in high O_2 concentration environment, is correlated with the surface elastic indentation modulus (EIT) of the polymer matrix, which increases due to the exposition to the environment and to thermo-oxidation effects (see also [22]). Past literature ([23]) showed the EIT can be directly correlated with the concentration of oxidation products, therefore the EIT can be taken as an oxidation tracer. Correlation between fatigue crack density and surface EIT values showed that environmental fatigue is mainly lead by surface embrittlement due to thermo-oxidation, taking place essentially at the microscopic scale, for all environmental conditions.

This work aims at characterizing and modelling the high-temperature (250°C) fatigue behaviour of C/polyimide 8-harness satin woven composites, in particular the development of damage related to cyclic mechanical mechanisms (fatigue) under controlled (temperature and gas) environment.

An experimental setup is specifically developed in order to perform fatigue tests under controlled environment (2 bar N_2, air, 2 bar O_2). Sample properties evolution during fatigue tests at 250°C are monitored using *in-situ* DIC, and damage assessment is provided by *ex-situ* μCT. Composite behaviour models are employed for rational understanding of the experimental results.

The work pairs Part I [24], in which extensive details about in-situ DIC, and damage assessment is provided by ex-situ μCT techniques are given, showing that these two techniques are effective and complementary for damage assessment under fatigue at high temperature under aggressive environment. The techniques and methods developed in Part I are here fully exploited for monitoring fatigue-creep-environment couplings. It is here important to stress that due to the peculiar type of loading (fatigue loads at high temperature under gaseous environment) non contact measurement techniques must be mandatorily be employed. Moreover the intrusiveness and the degradation of the measurement system itself constitute an issue *per se*, already extensively discussed in Part I [24].

The paper is organised as follows: Section 2 presents the material and the experimental approach, Section 3 illustrates the effect of the environment on high temperature fatigue, Section 4 presents a discussion on the effect of the environment, Section 5 presents the setup and the use of a model which is used for the understanding of experimental results and allows performing predictive simulations. Finally, Section 6 presents conclusions and perspectives.

2 – Material and experimental approach

The studied material is a carbon/polyimide T650-35/MVK-14 $[45]_6$ 8-harness satin woven composite material made by resin transfer moulding The matrix in this material has a glass transition temperature, about 325°C-335°C (DMA results), and the resin volume fraction in the composite is between 34% and 38%. Figure 1 gives a schematic illustration of the specimen and of the architecture of a unit cell and of the textile composite ply. The material properties provided by the supplier are reported in Table 1 [22]. Further details of the composite ply architecture and dimension are given in [24].

All the mechanical tests have been performed using the COMPTINN' test setup: this is an INSTRON 1251 equipped by a climatic chamber specifically developed to carry out mechanical tests in controlled environment (T_{MAX}: 350°C, p_{MAX}: 5 bar, environment: air, O_2, N_2). The climatic chamber does not allow using gauges for strain measurements, only non-contact techniques can be used for strain measurement. Further details about the experimental setup and the COMPTINN' test device are given in Part I of the article ([24]).

Tension-tension fatigue tests have been performed under three environmental conditions: air, 2 bar N_2 and 2 bar O_2. The load-piloted fatigue test is illustrated schematically in Figure 2, while the fatigue test parameters are resumed in Table 2.

DIC acquisition was carried out at fixed times during the fatigue test (*in-situ*). Fatigue tests were periodically interrupted to carry out intermediate quasi-static load/unload cycles and sample periodically removed from the test rig for μCT scans. Full details about the DIC and μ-CT experimental techniques are given in Part I of the article ([24]).

The output strain field from the CORRELA® software (see, for instance [24]-[26]) is quite heterogeneous. Several inhomogeneities of the strain field are due to several features, in the studied woven architecture the tow width is large enough to contain 4 data points. If some subsets fall on a resin rich region or on a tow or even on a crossover tow, the corresponding strain value could be different from the surrounding data points lying on the surface tows. Another source of inhomogeneity of the strain field is represented by cracks: since the employed DIC algorithm allows calculating only continuous strain field, cracks appear as large strain regions. To obtain strain values at the macroscopic scale at a given instant of a traction test an arithmetic mean over the whole stain field is calculated. This gives the same results of a virtual extensometer fixed at the upper and bottom sides of the painted region of the specimen.

Figure 3 illustrates a typical stress-strain curve obtained by averaging measured DIC strain fields during a traction loading-unloading curve. By this curve it is possible to extract ~~mesoscopic~~ macroscopic indicators of the material behaviour as will be shown later in Figure 5 and Figure 6; for instance, the longitudinal chord modulus along the traction direction (y), E_y^{ch}, the longitudinal secant modulus along the traction direction (y), E_y^{sec}, the hysteresis area below the whole stress-strain curve, A, and the permanent strain during fatigue, ε_{max_y}. ~~In addition, the secant shear modulus, G_{12}^{sec}, has been calculated using the maximum shear strain and the maximum shear stress values in the fibre direction for each load/unload cycle.~~

In addition, the secant shear modulus, G_{12}^{sec} defined as Eq.1, has been calculated using the maximum strain in the load direction and in the transversal one ($\varepsilon_x^{MAX}, \varepsilon_y^{MAX}$) and the maximum stress values (σ_y^{MAX}) for each load/unload cycle.

$$G_{12}^{sec} = -\frac{\sigma_y^{MAX}}{2\,(\varepsilon_x^{MAX} - \varepsilon_y^{MAX})} \qquad \text{(Eq.1)}$$

Referring to Figure 5 and Figure 6, the measured quantities are:

- the longitudinal elastic moduli, E_y^{ch}, is defined from the data points of the first stages of traction using the method reported in [27]: a chord modulus is calculated as the slope of a straight line fitting the corrected machine data points over the strain range 0.03%-0.13%. The secant properties are generally strongly affected by creep effects, so corrected data on movable head displacement have been used for "elastic" properties calculation;
- the longitudinal secant moduli, ~~E_y^{ch}~~ E_y^{sec}, has been calculated using the maximum longitudinal strain and the maximum longitudinal stress values for each load/unload cycle;
- the hysteresis area, A, is used to characterize the load/unload cycles in full, while the previous two properties characterize only the load stage. Since a residual strain is recorded at the end of the unload stage, the resulting hysteresis loop is not completely closed in the bottom side of the stress/strain graph. During fatigue, the magnitude of this residual strain

decreases and in the quasi-static load/unload cycle performed after ~170k cycles, the hysteresis loops seem to be perfectly closed;

- the fatigue maximum strain, ε_{max_y}, allows quantifying the creep/fatigue interaction during fatigue.

3 – Environmental effects on high temperature fatigue

3.1 – Preliminary traction tests

Two preliminary static traction tests have been performed to characterize the non-aged specimen behaviour at 250°C. During traction tests, DIC has been used to measure surface strain field using the DIC parameters reported in [24]. The tensile test results are illustrated in Figure 4. The stress values have been calculated by dividing the applied force by the cross section area of the virgin specimen, while the strain values plotted in the graph are the mean values issued from the DIC strain fields, as explained in [24]. ~~The description and the identification of the shear properties for woven composites is detailed in Appendix A.~~

The stress/strain curve of Figure 4 clearly shows that during traction the non-linearity in the material response increases as the applied load increases. At a value of stress σ_y = 136±2MPa the test has been interrupted because the strain grows up without load increasing (not reported in Figure 4), this load is used as Ultimate Tensile Strength (UTS) for the specimens. Some DIC strain fields, calculated during the traction test, are illustrated in Figure 4 on the traction stress/strain curve. As the load increases, high strain zones appear in the strain field. These regions tend to coalesce forming straight lines oriented in the direction parallel to the -45° tows. The high strain values can be correlated, as explained in [24], to the woven architecture or to cracks, the spatial resolution of the strain field does not allow separating these two features.

As explained in the Appendix A, the presented tensile test has been used in for matrix properties identification by using a microstructural FE model.

3.2 – Property evolution during fatigue

First three tests (one for each environmental condition) have been carried out, without any intermediary stop, until failure of the specimens. The effect of the environment on fatigue can be seen by looking at the number of cycles to rupture of the three samples (see Table 3). Table 3 indicates a significant life-reduction effect during fatigue in strongly oxidizing environmental test conditions (2 bar O_2), while the life duration of 2 bar N_2 and Air samples is of the same order of magnitude. This is related to the O_2 partial pressure in the testing environment: O_2 partial pressure in in the former environment is 10 times greater than the O_2 partial pressure in air. Finally, the latter environment is a inert environment for the tested material.

Following test have been performed using parameter in Table 2. During these interrupted fatigue tests the failure of the 2 bar O_2 specimen takes place at half of the prefixed test duration (330k cycles), while air and the 2 bar N_2 specimens arrive to the prefixed end of fatigue test without failing.

Typical longitudinal strain fields observed during load/unload cycles are shown in Figure 5 (after 1 Cycle- virgin sample – Figure 5a, after 230k Cycles – Figure 5b). For both the same stress levels, the strain fields during the load stage of the quasi-static load/unload cycle are similar in terms of mean strain pattern.

At the maximum stress level, the mean strain value encountered in the virgin specimen is higher than the value observed for the same specimen after 230k fatigue cycles. The same consideration could be made for the strain field relative to the end of the unload stage. The heterogeneity sources in the strain fields in Figure 5 a) are due to DIC algorithm errors and to the woven architecture, while in the case of the load/unload cycle reported in Figure 5 b) a further source of heterogeneity is related to cracks. As already explained in [24], for mechanical properties calculation, only the mean value of each strain field is plotted as a function of the applied stress. DIC data points have been interpolated using second degree polynomials to smooth the strain along time. Load and unload curves have been interpolated using two different polynomials and finally the area enclosed by the interpolating polynomials has been calculated.

Figure 6 a), b), c), d) illustrates, respectively, the evolution of the hysteresis area, A, of the secant shear modulus, G_{12}^{sec}, the chord longitudinal modulus, E_y^{ch}, the secant longitudinal modulus, E_y^{sec}, as a function of the number of cycles during fatigue. Dotted lines are manually drawn to show a general trend, for all properties. On the horizontal axis, cycle zero is first traction for the specimen.

The hysteresis area starts from a value of 10-15×10^4 J/m^3 at the beginning of fatigue and decreases until 2-5×10^4 J/m^3 after 6k-50k cycles. This last value is kept until the end of the test for the air and 2 bar N_2 specimen, while a slightly rise is seen for the 2 bar O_2 specimen just before the failure. This final rise for the 2 bar O_2 specimen, could be due to the stick-slip frictional sliding ([27], [28]).

After an increase from 2 to 3.5-4 GPa in the first thousands cycles, the shear secant modulus does not evolve for the air and 2 bar N_2 specimen, while a gradual decrease from ~200k cycles is observed for the 2 bar O_2 specimen until the end of the test.

For the three tested specimens the initial E_y^{ch} value is around 14 GPa, after 30k cycles E_y^{ch} decreases to 11-12 GPa, after that a slightly continuous reduction is observed for the three specimens until the end of the test. Dotted lines in Figure 6 c) represent the trend of the experimental data. These lines show a decrease rate different for the E_y^{ch} of the three specimens. The 2 bar O_2 specimen has the highest decrease rate, while the decrease rates of the 2 bar N_2 and air specimen are quite similar. On the initial value of the chord modulus a scatter is observed for the three specimens, besides only three specimen have been tested because the complexity and the duration of the tests, it follows that a statistical analysis on the obtained results is not practicable.

As for G_{12}^{sec}, an increase of the secant longitudinal modulus, E_y^{sec}, is observed in the early stage of fatigue and for the rest of the test a constant degradation rate is observed for the three tested specimens. In detail, the 2 bar O_2 specimen seems to start the degradation before to arrive to the stabilized value.

The difference between elastic and secant moduli is a measure of the non-linearity in the tensile longitudinal coupon response. The chord modulus reduction and the secant modulus increase in the first stage of fatigue could be linked to a damage development that does not give a rise in terms of non-linearity in the tensile response of the specimen, on the contrary the longitudinal response

becomes more linear and this is also supported by the decreasing of the hysteresis area. The stiffness degradation in the second stage of fatigue results in a rise of the difference between chord and secant moduli suggesting that damage introduces a non-linearity in the longitudinal direction that however is not detectable on the hysteresis curves. The first evolution stage of the chord and secant moduli may be mainly due to two phenomena that could act together:

- the former is fibre reorientation: for a woven composite material, loaded along an off-axis direction, a stiffening of the specimens could be present as a result of fibre rotation, as in [29] where the test temperature was higher than T_g of the composite's matrix. In [19] the same stiffening effect has been observed at test temperature lower than T_g for a carbon fibre/bismaleimide woven composite. For the authors the increase in stiffness was about 20%, and the magnitude of the fibre rotation, indirectly calculated from the permanent longitudinal deformation, was around 0.15°. In the graphs reported in Figure 6, a stiffening of the materials is noticeable only on the secant properties. The chord modulus decreases from the beginning to the end of the tests. Two reasons could clarify this evolution: the major effect of the damage on the evolution of the chord modulus in the first stage of fatigue, so, despite the stiffening due to fibre rotation, the softening effect linked to damage is more important. This could results in the linearization of the tensile longitudinal response seen in this fatigue stage (i.e. the secant modulus tends toward the value of the chord modulus). The second explanation is that the fibre rotations take place only after a threshold stress, so only in the high zone of the stress-strain curve there is a change;
- the second kind of phenomena taking place in the first step of fatigue, can be linked to the viscous nature of the matrix: the stiffening of the specimens could be due to a kinematic hardening of the matrix, as explained in [30] for an epoxy matrix during cyclic load. Recently, the fatigue data analysis of some authors focused on the ratcheting strain. This is the progressive accumulation of deformation while the materials are subjected to cyclic loading, especially under stress controlled mode with a non-zero mean stress ([31]).

The two discussed phenomena could be linked: as explained ever in [29], a plasticization of the resin regions results from the rotation of the fibre bundles that can lead, at a macroscopic level, to the same effect of a matrix hardening.

These phenomena are here introduced to give a possible interpretation of the general evolution of the obtained curves, but will be no longer investigated. In fact, all these evolutions are seen at the beginning of the tests when the environmental effect are not yet visible on properties evolution.

Some authors characterize the degradation of the tested specimens during fatigue studying the evolution of longitudinal strains (minimal, mean or maximal). The evolution of the maximum residual strain, ε_{max_y}, throughout the fatigue tests, issued from the data about the displacement of the movable part of the test machine, is reported in Figure 7.

The environmental effect is remarkable in Figure 7, where in the early stage of fatigue, the ε_{max_y} trend is the same for the three specimens. After an initial increase, the environment begins to affect the response of the specimens and the three specimens take three different evolutions. For the air and 2 bar N_2 specimen, a slightly increase of the maximum strain is observed until the end of test. For the 2 bar O_2 specimen, after the initial evolution, the maximum strain grows up rapidly up to the specimen failure. As will be shown in section 3.4,the evolution of the ε_{max_y} during fatigue can be

viewed as the sum of three contributions: firstly, a strain linked to damage development during fatigue, then a second terms related to creep during fatigue and finally a third term related to the elasto-plastic deformation dependent on the maximum fatigue load.

Summarising, in Figure 6 and Figure 7 three evolution stages are discernible:

- firstly, a rapid evolution toward a steady state, clearly remarkable for E_y^{sec}, G_{12}^{sec}, A and ε_{max_y},
- a steady state that, for the 2 bar N_2 and air specimen, persists until the end of the fatigue test,
- finally, a gradual evolution of the properties from the end of the second stage up to the end of fatigue. This last evolution stage is clearly visible looking at the 2 bar O_2 specimen related graphs.

The most important evidence issued from these graphs is the role of the environment on fatigue behaviour. In fact, after the first evolution stage, completed within 70k cycles (i.e. ~10 hours), the evolution of the three specimen properties begins to differ from each other. In particular for the 2 bar N_2 specimen, after the initial evolution, the longitudinal chord modulus slightly decreases, while the secant modulus does not change until the end of the test. For the air specimen a degradation is observed for both chord and secant moduli and finally; except for the chord longitudinal modulus, for the 2 bar O_2 the second stage of fatigue is not easy to detect on the graphs, a continuous loss of longitudinal properties is detected until failure but, until 100k-150k cycles to failure, the hysteresis area evolution does not suggest an increase in specimen energy dissipation.

3.3 – Damage evolution during fatigue

Extensive details about the damage measurement during fatigue have been provided in [24], both for DIC and μCT techniques.

Here, only some remarks on the observed damage scenario will be done, by presenting some μCT scan and segmentation results.

An exterior ply and the relative segmentation are illustrated in Figure 8. The non-segmented image is shown on the left; in this image cracks in the tows oriented along the -45° direction are clearly visible as little cracks in 0° direction and, uniquely in the crossover regions, cracks in the tows oriented along the +45° direction.

Using the segmentation procedure described in [24], the result of segmentation is reported in the central image of Figure 8, where the 0° cracks are in red, -45° cracks in blue and finally, +45° cracks in green. The segmented cracks are illustrated in the right side of Figure 8, where the 3D ply reconstruction is not reported. The majority of blue cracks on the right side in Figure 8 are continuous cracks and not all the cracks reach the lateral edges of the ply. Observing the surface of the specimen it is not possible to know if, in the crossover regions, the cracks in the -45° tows are interrupted or not. A zoom of the segmentation proposed in Figure 8 is reported in Figure 9.

In Figure 9 +45° cracks are shorter than the -45° ones and concentrated where the -45° cracks are more developed or close to the lateral edges of the ply. Three regions where the +45° crack density is high are zoomed and enclosed in dotted lines. Chronologically, the formation of +45° cracks far from the edges, is subsequent to the formation -45° cracks for the external ply in Figure 9.

The segmentation allows following the path of these cracks. A complete description of the crack location inside the woven is reported in Figure 10.

Figure 10 shows a representative region of a damaged external woven ply. The damage scenario described in these pictures is the same for all the tested specimens. In Figure 10 a) 4 tows are identified using dotted lines: the tows from 1 to 3 are surface tows aligned along the -45° direction, while the tow 4 is a +45 tow belonging to the same external ply.

The segmented cracks are illustrated in Figure 10 b), this figure clearly shows three different kind of cracks:

- 0° cracks (in red) are located in the resin rich regions and the direction of these cracks is normal to the direction of the applied load;
- -45° cracks (in blue) are aligned along the -45° direction and are located inside the -45° tows. In Figure 10 the path of the -45° crack, named Crack1, is shown: by using the cutting planes slice +45° from 1 to 3, one can see that this intra-tow crack propagates in the Tow1 also across the crossover region, where Tow1 passes under Tow4;
- +45° cracks (in green) are aligned along the +45° direction and are located inside the +45° tows. In Figure 10 the path of the +45° crack, named Crack2, is shown: by using the cutting planes slice -45° from 1 to 3, one can see that this intra-tow crack propagates in the Tow4 across the crimp region and has a propagation also in the tow regions that are not on the visible surface. This is shown by the slice-45°(1) and slice-45°(3) where Crack2 propagates also under Tow3 and Tow2 respectively.

A potential conclusion issued from the analysis of Figure 9 and Figure 10 is that in the external plies (that are the biggest two surfaces directly exposed to the testing environment) the -45° cracks propagate in the crimp region only after an extensive propagation in the straight zone of the tow between two crimp regions, while +45° cracks onset after the apparition of -45° cracks.

A chronological description of the crack onset and propagation is now presented for the three test conditions. For simplicity only an exterior ply are presented for each specimen, bearing in mind that for each test condition the damage process of all the external plies is the same.

The conclusions issued from the observation of the segmentation results are detailed in the following sub-paragraphs. The environmental conditions affect both damage scenario and damage extension. The presence of regions, in the observed specimens, where the damage is less or more extended than other ones, highlights the heterogeneous nature of the damage distribution and hence the importance in analysing and study a large specimen region to correctly characterize the damage process.

Looking at the μCT results, two mainly aspects of the damage could be remarked. The former is the specific damage evolution in the different plies of each specimen. In all the external plies, the first damage form are the cracks in the surface tows direction of the plies. These appear in the specimens as multiple cracks in the same tow and tend to coalesce in a single crack. The early crack development in the exterior ply is already reported in [32]; for the authors this could be due to the major undulation of the exterior tows respect the inner ones or, to the better deformability of the exterior plies if compared to the interior ones, during load. The presence of +45° cracks is often related to the presence of -45° ones and rarely they onset from the lateral edges of the specimens.

In the internal plies the damage is less important than the external ones. The presence of cracks in -45° is important as the presence of cracks in +45° direction and no 0° cracks are detected.

The second and the most relevant aspect of μCT results, is the observation of the differences in damage scenario for the three environmental conditions. In the external plies the formation of +45° cracks is strongly dependent on the test conditions: in terms of +45° crack volume, after 170k cycles the difference for the three specimens is not relevant, while at 550k cycles there is a great gap for the external plies damaged volume. Since the formation, propagation/multiplication of -45° cracks in an exterior ply seems to be affected by the environmental test conditions, and the presence of +45° cracks related to the presence of -45° cracks, under severe environmental conditions (2 bar O_2) the +45° cracks are more numerous compared to +45° cracks in the external plies of the air and 2 bar N_2 specimen. For the internal plies, an important environmental effect is the preferential location for crack onset: for the 2 bar N_2 specimen the cracks presence seem to be linked to internal defects and/or stress concentration zones. For air and 2 bar O_2 specimen the cracks onset mainly on the lateral edges i.e. the surfaces directly exposed to the environment.

In order to compare the detected cracks, a global quantitative evaluation of the volumetric crack density during fatigue is proposed. For each μCT scan, the specimen volume (V^{TOT}) and the segmented cracks volume (V^{CRACK}) are calculated using the label analysis tool in Avizo9®. The volumetric crack density $D^{\mu CT}$ is hence defined from Eq. 2

$$D^{\mu CT} = \frac{V^{CRACK}}{V^{TOT}} \quad \text{(Eq.2)}$$

The evolution of $D^{\mu CT}$ is reported in Figure 11, it can be seen that for air and 2 bar N_2 specimen tested the damaged volume is quite similar for Test1 and Test2 specimen. This support the reproducibility of the tests. For the 2 bar O_2 specimens there is a remarkable difference because the specimen of Test1 fails at 330k cycle and at the failure the damaged volume is 1.1% of the total specimen volume. The Test2 specimen fails at 550k cycles with 2.1% of damaged volume. An important evidence is that the ratio between the numbers of cycle at failure of the two 2 bar O_2 specimens is 1.6, while the ratio between damaged volumes at failure is 1.9. This similarity could be due to a direct environmental effect on the damage evolution, the specimen more exposed to environmental condition is more damaged than the specimen less exposed. If the damage level in the specimen is not an indicator of the health of the specimen, some other phenomena are correlated to the failure of the specimens such as fatigue-creep interaction. As discussed in [23], the uncertainty linked to the crack thickness in segmentation process can lead do under or over estimate the crack volumes. Moreover, the use of the crack length for damage characterization allow to compare damage extent measured by using two different techniques: DIC and μCT.

As described in [23], the image processing procedure allows describing crack distribution semi-ply-by-semi-ply and for each tow direction, identifying a stacking sequence of semi-plies having approximately the thickness of a tow, and in which the cracks have the tow orientation. The total crack length (L) can be used to evaluate the damage level in each semi-ply of the sample (Figure 12). Figure 12 illustrates the semi-ply-by-semi-ply crack length distribution as a result of the segmentation procedure for three samples tested at 250°C under different environments (2 bar N_2, air, 2 bar O_2) for different cycle numbers. The cracks are mainly narrowed on the external semi-plies

(Ply1 -45° and Ply6 +45°), while for the inner plies the crack length distribution is quite homogeneous.

With respect to the inert environment (2 bar N_2), the effect of thermo-oxidation at high temperature (under air or 2 bar O_2 environment), promotes higher crack density. Crack length is higher in the eternal plies directly exposed to the environment.

Another advantageous indicator of damage is represented by the crack density in a semi-ply (Eq.3)

$$D_{SP}^{\mu CT} = \frac{L_{SP}^{CRACK}}{L_{SP}} \quad \text{(Eq.3)}$$

where the subscript SP stands for Semi-Ply, where L_{SP}^{CRACK} is the sum of the crack length (along the tow direction) and L_{SP} is the length of the zone observed by μCT (around 42.3 mm).

The three measures of damage will be useful in the following.

3.4 – Properties vs. Damage evolution during fatigue

The macroscopic properties evolution is here correlated to matrix crack volume issued by μCT. Figure 13 shows the evolution of the hysteresis area, A, Figure 13 a), of the secant shear modulus, G_{12}^{sec}, Figure 13 b), of the longitudinal chord modulus, E_y^{ch}, Figure 13 c), and of the longitudinal secant modulus, E_y^{sec}, Figure 13 d), as a function of $D^{\mu CT}$.

As $D^{\mu CT}$ increases, no noticeable evolution of A is seen. Only for the 2 bar O_2 specimen a slight rise of A occurs when $D^{\mu CT}$ is higher than 2%. As for the previous graph, no apparent link exists between G_{12}^{sec} and $D^{\mu CT}$, only for the 2 bar O_2 specimen an important degradation of G_{12}^{sec} is seen when $D^{\mu CT}$ is higher than 2%. A continuous degradation of the chord modulus is observed as the $D^{\mu CT}$ increases. The three data series seem to lie to the same straight, the proposed trend in dotted line in Figure 13 c) resumes the supposed linear evolution. Despite this, the points of the three specimens are not perfectly aligned on this straight line. As for A and G_{12}^{sec} there is not a clear evolution of E_y^{sec} as the cracked volume increases.

The evolution of the maximal residual strain, ε_{max_y}, illustrated in Figure 7 can be schematically described by Eq.4

$$\varepsilon_{max\_y} = \varepsilon_c + \varepsilon_{D\_y} + \varepsilon_{vep\_y}^{f} \quad \text{(Eq.4)}$$

in which ε_c is a term related to 'pure' creep, ε_{D_y} is a term related to damage and $\varepsilon_{vep\_y}^{f}$ is a term related to creep-fatigue interaction.

The ε_c term can be expressed as in Eq.5

$$\varepsilon_c = \varepsilon_0(\sigma) + K\sigma^m t^n \quad \text{(Eq.5)}$$

Which expresses a classic Nutting approximation fitting [33]. The parameters of this fitting function, ε_0, K, m and n, can be found by performing equivalent creep tests at constant stress corresponding to the average fatigue stress for the duration of a fatigue test. Table 4 resumes the results of this fitting for the three tested environments while creep test results and interpolation are shown in Figure 14.

In order to separate the two contributions $\varepsilon_{D\_y} + \varepsilon^{f}_{vep\_y}$ for the three specimens, the evolution of the $\varepsilon_{D\_y} + \varepsilon^{f}_{vep\_y}$ as a function of the global volumetric crack density is plotted in Figure 15. The initial value on the graph could be related to an instantaneous strain accumulation linked to the maximum fatigue load and not to damage. Starting from this initial strain value, a linear relation can be assumed between the μCT measured damage and the macroscopic longitudinal strain evolution. A master curve having the form reported in Eq.6 can be plotted to describe the evolution of the strain $\varepsilon_{D\_y} + \varepsilon^{f}_{vep\_y}$ independently on the test environment. The value on the vertical axis in Figure 15, for $D^{\mu CT} = 0$, could be associated to the terms $\varepsilon^{f}_{vep\_y}$ in the presented analysis, it is supposed to not evolve during fatigue and its value is $\varepsilon^{f}_{vep\_y} = 0.8$. The slope of the straight line, parameter B in Eq.6, gives the weight of the volumetric crack density on the damage related strain. This slope is not dependent on the environmental conditions and for the graph in Figure 15, its value is B= 1.34.

$$\varepsilon_{D\_y} + \varepsilon^{f}_{vep\_y} = B \times D^{\mu CT} + 0.8 \qquad \text{(Eq.6)}$$

4 – Discussion on the effect of the environment

As noted in the introductory section, the observed behaviour has its origin from the phenomena taking place at the micro-scale, in turn affected by the environment. In fact (Figure 16) the exterior plies of the woven specimens represent two large surfaces potentially degraded by the thermo-oxidation process, in which matrix degradation may promote the acceleration of damage evolution and have a strong impact on the off-axis samples mechanical behaviour. Since environmental phenomena can be essentially considered as surface phenomena, the kinetic of ageing can be described by the value of the matrix elastic indentation modulus (EIT) measured by nanoindentation at the external sample surface (EIT_{MAX}) or by its adimensional counterpart, γ_{MAX}, defined by (see also [22] [34])

$$\gamma_{MAX} = \frac{EIT_{MAX} - EIT_0}{EIT_0} \qquad \text{(Eq.7)}$$

EIT_0 is the elastic indentation module of the virgin resin. The evolution of γ_{MAX} as a function of the ageing time for the specimens aged in air and in 2 bar O_2 is reported in Figure 17 a). An interpolation function (Eq.8) has been used to fit the experimental data, plotted in continuous line in Figure 17 a) for each ageing condition with the parameters reported in Table 5.

$$\gamma_{MAX}(250°C, p, t) = 0.75 - 0.4\exp\left(-\frac{t}{\tau_1(p)}\right) - 0.35\exp\left(-\frac{t}{\tau_2(p)}\right) \qquad \text{(Eq.8)}$$

By looking at Table 5, the acceleration of the oxidizing process obtained using 2 bar O_2 can be quantified using a scaling factor, λ, equal to around 6, that is, an average value between the two characteristic time ratios in Table 5. By using the reduced time, $t^* = \lambda t$, Eq. 7 becomes

$$\gamma_{MAX}(250°C, p, t) = 0.75 - 0.4\exp\left(-\frac{t^*}{7000}\right) - 0.35\exp\left(-\frac{t^*}{310}\right) \quad \text{(Eq.9)}$$

~~The obtained master curve is reported in Figure 16 b)~~

The evolution of γ_{MAX} reported in Figure 17 a) for two different environments that are 2 bar O_2 and Air can be, hence, described by the master curve of Eq.9 and graphically reported in Figure 17 b).

The evolution of the macroscopic properties, the hysteresis area, A, the secant shear modulus, G_{12}^{sec}, the chord longitudinal modulus, E_y^{ch}, the secant longitudinal modulus, E_y^{sec}, as function of the oxidation tracer (aging parameter), γ_{MAX}, are plotted in Figure 18 (respectively, 18 a),b),c),d)). Figure 19, Figure 20 and Figure 21 illustrate, respectively, the evolution of ε_{max_y}, ε_{D_y} and L as a function of the aging parameter, γ_{MAX}.

The master curves presented in this paragraph show that the ageing parameter can be used as an index to describe the oxidation effects on the woven composite. This scaling parameter, in particular, perfectly matches the evolution of the elastic longitudinal modulus and the damage evolution. Consequently, an acceleration of the fatigue test performed in air can be obtained by testing specimens in 2 bar O_2. Looking the master curves in Figures 19-21, it could be concluded that the thermo-oxidation process of the resin promotes the damage development on the exposed surfaces accelerating the specimen degradation.

Based on this result, a test protocol for accelerated environmentally-assisted fatigue can be proposed. The protocol consists of two phases, namely:

- identification of the ageing parameter evolution (γ_{MAX}) from indentation tests on the surface of pure resin samples under different environmental conditions: a reference condition, under air at atmospheric pressure, and an accelerated condition, under a certain pressure of pure oxygen. This tests allow identifying the scale factor between the reference and the accelerated environmental condition;

- realization of environmentally-assisted fatigue tests under the same accelerated environmental conditions. This allows obtaining the same results as those obtained under reference environmental conditions, in less experimental time.

5 – Ply-by-ply discretization model

The sample architecture (Figure 1) allows identifying a ply-by-ply discretization, characterized by elementary woven plies with satin texture arranged in a laminated stacked sequence (Figure 1 b)).

On the other hand, the volumetric crack distribution revealed by μCT scans and related segmentation allows identifying a semi-ply-by-semi-ply through-the-thickness crack distribution (Figure 12), the thickness of a semi-ply being the thickness of a tow which is also the thickness (height) of a crack. Semi-plies are further identified by the orientation or their respective tows which is also the fibre direction and is taken as semi-ply direction 1.

Moreover, μCT scans (and DIC in the external plies) are able to identify an oriented pattern of microcracks, for each semi-ply (Figures 8-10) with density defined as in Eq.3.

Cracks are aligned along the tow direction (semi-ply direction 1) and open along the direction transverse to the tow (semi-ply direction 2): it is therefore plausible to think that they have an effect essentially on the semi-ply transverse direction (as they directly affect the transverse compliance by crack opening) and the in-plane shear behaviour (as cracks may slide with friction in their plane).

It is therefore plausible to construct a semi-ply-based plane stress damage-dependent constitutive law and considering the sample mechanical response as the response of a stacked sequence of damageable semi-plies, having in mind the tows orientation (semi-ply direction = direction 1), the directionality of cracks (along direction 1) and using the lamination theory for constructing the response of the laminate (see also Appendix B). The damage-dependent constitutive law of the semi-ply is therefore of the form

$$\boldsymbol{\sigma}_{SP} = \mathbf{Q}_{SP}(D)(\boldsymbol{\varepsilon} - \boldsymbol{\varepsilon}_{cf} - \boldsymbol{\varepsilon}_{th}) \tag{Eq.10}$$

in which $\boldsymbol{\sigma}_{SP}$ is the semi-ply stress, $\boldsymbol{\varepsilon}$ the total strain, $\boldsymbol{\varepsilon}_{cf}$ and $\boldsymbol{\varepsilon}_{th}$ are, respectively, the inelastic strain related to creep or creep-fatigue interaction and strain of thermal origin (such as those occurring due to material manufacturing at high temperature). In the present case, $\boldsymbol{\varepsilon}_{cf}$ can be taken to the experimentally measured creep stress (see Section 3.4), $\boldsymbol{\varepsilon}_{cf}$=($\varepsilon_{max\_y}, 0, 0$), while $\boldsymbol{\varepsilon}_{th}$can be calculated from the knowledge of the matrix Coefficients of Thermal Expansion by the employment of FE models (see Appendix A). $\mathbf{Q}_{SP}(D)$ represents the semi-ply damage dependent plane stress stiffness matrix given by (in the 1, 2 – tow, transverse-to-tow reference frame)

$$\mathbf{Q}_{SP}(D) = \begin{pmatrix} \frac{E_{11}}{1-\nu_{12}\nu_{21}} & \frac{\nu_{21}E_{11}}{1-\nu_{12}\nu_{21}} & 0 \\ \frac{\nu_{21}E_{11}}{1-\nu_{12}\nu_{21}} & \frac{E_{22}(1-D_{22})}{1-\nu_{12}\nu_{21}} & 0 \\ 0 & 0 & G_{12}(1-D_{12}) \end{pmatrix} \tag{Eq.11}$$

in which, for each semi-ply

$$D_{22} = \beta D_{SP}^{\mu CT}$$
$$D_{12} = cD_{22} \tag{Eq.12}$$

β and c are interaction parameters. By this way damage acts in a direction perpendicular to that of the tows (D_{22}) and in shear (D_{12}). Following an approach also found in [35] for satin textile laminates, the stiffness matrix of a ply is given by the algebraic weighted average of the semi-plies: for instance, for the ±45° ply one would write

$$\mathbf{Q}_{P}^{\pm 45} = n_{+45}\mathbf{Q}_{SP}^{+45} + n_{-45}\mathbf{Q}_{SP}^{-45} \quad \text{(Eq.13)}$$

To each semi-ply is associated an elastic-damage complementary energy density of the form

$$e_{SP}^{*} = \frac{1}{2}\left[\frac{\sigma_{11}^2}{E_{11}} + \frac{\sigma_{22}^2}{E_{22}(1-D_{22})} - \frac{2\nu_{12}}{E_{11}}\sigma_{11}\sigma_{22} + \frac{\sigma_{12}^2}{2G_{12}(1-D_{12})}\right] \quad \text{(Eq.14)}$$

from which it is possible to calculate by derivation the variables (thermodynamic forces) needed to model the kinetic laws of evolution (which can be improperly referred as energy release rates)

$$Y_{22} = \frac{\partial e_{SP}^{*}}{\partial D_{22}} = \frac{\sigma_{22}^2}{2E_{22}(1-D_{22})^2}$$

$$Y_{12} = \frac{\partial e_{SP}^{*}}{\partial D_{12}} = \frac{\sigma_{12}^2}{2G_{12}(1-D_{12})^2} \quad \text{(Eq.15)}$$

Figure 22 illustrates the evolution of the longitudinal chord modulus, E_y^{ch}, during fatigue, with increasing the number of cycles, including the fitting obtained by the employment of the laminated semi-ply-by-semi-ply damage-dependent model (dotted lines in Figure 22). A progressive reduction of the moduli is measured for the three environmental conditions: with respect to the inert environment (2 bar N_2) the kinetic of property decrease is more marked under air and under 2 bar O_2, oxidizing conditions promote more rapid degradation related to damage evolution. The laminated semi-ply-by-semi-ply damage-dependent model can follow this evolution for a unique value of the parameters β and c. The values for these parameters have been found during the presented experimental campaign by fitting experimental results; found values are β=0.035 and c=1 (see also Appendix B for more details).

Once identified, the model can be employed for the calculation of the thermodynamic forces and to identify the kinetics of damage evolution. For the sake of illustration, Figure 23 presents the evolution of the thermodynamics forces, Y_{22} and Y_{12}, in the +45° ply, as a function of number of cycles. The thermodynamic forces increase with increasing number of cycles. Moreover, the highest values of Y_{22} and Y_{12} are calculated for the 2 bar O_2 environmental condition.

It is interesting to note that all model properties can be calculated (or parametrized) as a function of the oxidation tracer, γ_{MAX}, instead of time, to take explicitly into account the effect of the environment.

6 – Conclusions

This paper has been devoted to the study of high temperature fatigue of Carbon/polyimide 8-harness satin woven composite materials. Traction-traction (R=0.1) fatigue tests at 250°C are carried out on Carbon/polyimide [45]6 8-harness satin woven composites under three different environments (air, 2 bar N_2, 2 bar O_2), in particular the environmental effects occurring during high temperature fatigue. Strain, mechanical properties and damage evolution have been characterized by Digital Image Correlation (DIC) and μ-Computed Tomography (μCT) techniques. The damage description has been formalised in a way that can be naturally integrated within the context of damage-dependent behaviour models. The effect of the environment has been assessed through a description of thermo-oxidation phenomena occurring at high temperatures

It has been shown that:

- the environment plays an important role on the evolution of damage and of the macroscopic properties during fatigue,
- the effects of the environment can be described through the description of the ageing parameter, γ_{max} which is the adimensional counterpart of the elastic indentation modulus measured on the external sample surface (EIT_{max}) and whose kinetics is an indicator of thermo-oxidation evolution on the sample surface,
- for the material architecture used in this study (2D textile composite) the employment of a ply-by-ply discretization model integrating the kinetics of damage as explicitly measured by μCT and possible viscoplastic effects due to creep-fatigue interaction is sufficient to have an accurate description of material property evolution during fatigue. The model can be useful to calculate energy release rate values as a function of the number of cycles,
- the realisation of environmentally-assisted fatigue test must necessarily be carried out under accelerated environmental conditions, in order to allow the property evolution due to accelerated fatigue be correlated to property evolution due to the effect of the environment. The scale factor between reference and accelerated environmental conditions can be accurately determined by looking at the evolution of the ageing parameter γ_{max} under reference and accelerated conditions.

Acknowledgement

This work was partially funded by the French Government program "Investissements d'Avenir" (EQUIPEX GAP, reference ANR-11-EQPX-0018). The research subject carried out within this research program falls within the research themes of the French Government program "Investissements d'Avenir" (LABEX INTERACTIFS, reference ANR-11-LABX- 0017-01). The authors would like to thank SAFRAN Nacelles for providing the composite material used in this work. Finally, we acknowledge the Poitou-Charentes Region (France) for funding the PhD Thesis of Federico Foti.

References

[1] M. Kashtalyan and C. Soutis, "Stiffness degradation in cross-ply laminates damaged by transverse cracking and splitting" *Compos. Part A Appl. Sci. Manuf.*, vol. 31, no. 4, pp. 335–351,

2000.

[2] V. Carvelli, A. Jain, and S. V. Lomov, *Fatigue of Textile and Short Fiber Reinforced Composites*, Wiley. 2017.

[3] N. Takeda and S. Ogihara, "Initiation and growth of delamination from the tips of transverse cracks in CFRP cross-ply laminates" *Compos. Sci. Technol.*, vol. 52, no. 3, pp. 309–318, 1994.

[4] J. M. Berthelot and J. F. Le Corre, "Statistical analysis of the progression of transverse cracking and delamination in cross-ply laminates" *Compos. Sci. Technol.*, vol. 60, no. 14, pp. 2659–2669, 2000.

[5] A. S. D. Wang, N. N. Kishore, and C. A. Li, "Crack development in graphite—epoxy cross-ply laminates under uniaxial tension" *Compos. Sci. Technol.*, vol. 24, no. 1, pp. 1–31, Jan. 1985.

[6] T. Osada, A. Nakai, and H. Hamada, "Initial fracture behavior of satin woven fabric composites" *Compos. Struct.*, vol. 61, no. 4, pp. 333–339, 2003.

[7] C. Rakotoarisoa, "Prévision de la durée de vie en fatigue des composites à matrice organique tissés interlock" PhD Thesis, UNIVERSITE DE TECHNOLOGIE DE COMPIEGNE, 2013. https://tel.archives-ouvertes.fr/tel-01073017/document

[8] V. Carvelli and S. V. Lomov, *Fatigue of Textile Composites*. Elsevier, 2015.

[9] S. Daggumati, I. De Baere, W. Van Paepegem, J. Degrieck, J. Xu, and S. V. Lomov, "Local Damage in a 5 – Harness Satin Weave Composite Under Static Tension : Part I - Experimental Analysis" *COMPOSITES SCIENCE AND TECHNOLOGY*, vol. 71, no. 8. Elsevier, pp. 1–24, 2011.

[10] B. Yu, R. Blanc, C. Soutis, and P. J. Withers, "Evolution of damage during the fatigue of 3D woven glass-fibre reinforced composites subjected to tension-tension loading observed by time-lapse X-ray tomography" *Compos. Part A Appl. Sci. Manuf.*, vol. 82, pp. 279–290, 2016.

[11] D.-Y. Song and N. Otani, "Approximate estimation of fatigue strength of polymer matrix composites by material properties" *Mater. Sci. Eng.*, vol. 254, pp. 200–206, 1998.

[12] S. D. Pandita, G. Huysmans, M. Wevers, and I. Verpoest, "Tensile fatigue behaviour of glass plain-weave fabric composites in on- and off-axis directions" *Compos. - Part A Appl. Sci. Manuf.*, vol. 32, no. 10, pp. 1533–1539, 2001.

[13] S. V. Lomov *et al.*, "Full-field strain measurements for validation of meso-FE analysis of textile composites" *Compos. Part A Appl. Sci. Manuf.*, vol. 39, no. 8, pp. 1218–1231, 2008.

[14] G. Nicoletto, G. Anzelotti, and E. Riva, "Mesoscopic strain fields in woven composites: Experiments vs. finite element modeling" *Opt. Lasers Eng.*, vol. 47, no. 3–4, pp. 352–359, 2009.

[15] M. Mehdikhani, M. Aravand, B. Sabuncuoglu, M. G. Callens, S. V. Lomov, and L. Gorbatikh, "Full-field strain measurements at the micro-scale in fiber-reinforced composites using digital image correlation" *Compos. Struct.*, vol. 140, pp. 192–201, 2016.

[16] J. Pazmino, V. Carvelli, and S. V. Lomov, "Micro-CT analysis of the internal deformed geometry of a non-crimp 3D orthogonal weave E-glass composite reinforcemen" *Compos. Part A Appl. Sci. Manuf.*, vol. 61, pp. 76–83, 2014.

[17] M. Barburski, I. Straumit, X. Zhang, M. Wevers, and S. V. Lomov, "Micro-CT analysis of

internal structure of sheared textile composite reinforcement" *Compos. Part A Appl. Sci. Manuf.*, vol. 73, pp. 45–54, 2015.

[18] S. M. Sisodia, S. C. Garcea, a. R. George, D. T. Fullwood, S. M. Spearing, and E. K. Gamstedt, "High-resolution computed tomography in resin infused woven carbon fibre composites with voids" *Compos. Sci. Technol.*, vol. 131, pp. 12–21, 2016.

[19] J. Montesano, M. Selezneva, Z. Fawaz, C. Poon, and K. Behdinan, "Elevated temperature off-axis fatigue behavior of an eight-harness satin woven carbon-fiber/bismaleimide laminate" *Compos. Part A Appl. Sci. Manuf.*, vol. 43, no. 9, pp. 1454–1466, 2012.

[20] M.C. Lafarie-Frenot, S. Rouquié, N.Q. Ho and V. Bellenger, "Comparison of damage development in C/epoxy laminates during isothermal ageing or thermal cycling" *Compos. Part A Appl. Sci. Manuf.*, vol. 37, pp. 662-671, 2006.

[21] F. Foti, M. Gigliotti, Y. Pannier, D. Mellier and M.C. Lafarie-Frenot, "The Effect of the Environment on High Temperature Fatigue of Cross-Ply C/Epoxy Laminated Composites" *Compos. Struct.*, vol. 202, pp. 924-934, 2018.

~~[22] M. Minervino, "Effets de la thermo-oxydation sur le comportement mécanique de matériaux composites pour applications aéronautiques" PhD Thesis, ENSMA, 2013.~~

[22] M. Minervino, "Effets de la thermo-oxydation sur le comportement mécanique de matériaux composites pour applications aéronautiques", Thèse Mécanique des solides, des matériaux, des structures et des surfaces, ENSMA, 2013. https://tel.archives-ouvertes.fr/tel-00926658/document

[23] L. Olivier, N. Q. Ho, J. C. Grandidier, and M. C. Lafarie-Frenot, "Characterization by ultra-micro indentation of an oxidized epoxy polymer: Correlation with the predictions of a kinetic model of oxidation," *Polym. Degrad. Stab.*, vol. 93, no. 2, pp. 489–497, 2008.

~~[24] F. Foti, Y. Pannier, D. Mellier and M. Gigliotti, "High Temperature Fatigue of Carbon/Polyimide 8-harness Satin Woven Composites. Part I: Digital Image Correlation and μ-Computed Tomography Damage Characterization" Int. J. Fatigue, Submitted, 2019.~~

[24] Y. Pannier, F. Foti and M. Gigliotti, "High Temperature Fatigue of off-axis Carbon/Polyimide 8-harness Satin Woven Composites. Part I: Digital Image Correlation and μ-Computed Tomography Damage Characterization" Composite Structures, Submitted, 2019.

[25] M. Bornert *et al.*, "Assessment of Digital Image Correlation Measurement Errors: Methodology and Results" *Exp. Mech.*, vol. 49, no. 3, pp. 353–370, Jun. 2009.

[26] J. C. Dupré, P. Doumalin, H. A. Husseini, A. Germaneau, and F. Brémand, "Displacement Discontinuity or Complex Shape of Sample: Assessment of Accuracy and Adaptation of Local DIC Approach" *Strain*, vol. 51, no. 5, pp. 391–404, 2015.

[27] S. Topal, L. Baiocchi, A.D. Crocombe, S.L. Ogin, P. Potluri, P.J. Withers, M. Quaresimin, P.A. Smith, M.C. Poole and A.E. Bogdanovich "Late-stage fatigue damage in a 3D orthogonal non-crimp woven composite: An experimental and numerical study" *Compos. Part A Appl. Sci. Manuf.*, vol. 79, pp. 155–163, 2015.

[28] E. Kristofer Gamstedt, O. Redon and P. Brøndsted "Fatigue Dissipation and Failure in Unidirectional and Angle-Ply Glass Fibre/Carbon Fibre Hybrid Laminates" *Key Engineering Materials*, vol. 221-222, pp. 35–48, 2002.

[29] W. Albouy, B. Vieille, and L. Taleb, "Influence of matrix ductility on the high-temperature fatigue behaviour of quasi-isotropic woven-ply thermoplastic and thermoset laminates" *Compos. Part A Appl. Sci. Manuf.*, vol. 67, pp. 22–36, 2014.

[30] H.S. da Costa Mattos and S. de Abreu Martins, "Plastic behaviour of an epoxy polymer under cyclic tension" *Pol. Test.*, vol. 32, pp. 1-8, 2013.

[31] Z. Zhang, X. Chen and Y. Wang, "Uniaxial ratcheting behavior of polytetrafluoroethylene at elevated temperature" *Pol. Test.*, vol. 29, pp. 352–357, 2010.

[32] B. Yu, R. Blanc, C. Soutis, P.J. and Withers "Evolution of damage during the fatigue of 3D woven glass-fibre reinforced composites subjected to tension-tension loading observed by time-lapse X-ray tomography" *Compos. Part A Appl. Sci. Manuf.*, vol. 82, pp. 279–290, 2016.

[33] P. Nutting "A study of elastic viscous deformation" *Proceedings of the American Society for Testing Materials*, XXI, pp. 1162–1171, 1921.

[34] M. Gigliotti, M. Minervino, M. C. Lafarie-Frenot, and J. C. Grandidier, "Effect of Thermo-oxidation on the local mechanical behaviour of epoxy polymer materials for high temperature applications," *Mech. Mater.*, vol. 101, pp. 1339–1351, 2016.

[35] Y. Thollon and C. Hochard, "A general damage model for woven fabric composite laminates up to first failure," *Mech. Mater.*, vol. 41, no. 7, pp. 820–827, 2009.

~~[36] C.T. Herakovich. (1998). Mechanics of Fibrous Composites. (I. John Wiley & Sons, Ed.) (First)~~

[36] Y. Sinchuk, Y. Pannier, M. Gueguen, D. Tandiang, and M. Gigliotti, "Computed-tomography based modeling and simulation of moisture diffusion and induced swelling in textile composite materials," Int. J. Solids Struct., pp. 1–9, 2017.

[37] C.T. Herakovich. (1998). Mechanics of Fibrous Composites. (I. John Wiley & Sons, Ed.) (First)

[38] Berthelot, J. M., El Mahi, A., & Leblond, P. (1996). Transverse cracking of cross-ply laminates: Part 2. Progressive widthwise cracking. Composites Part A: Applied Science and Manufacturing, 27(10), 1003–1010. https://doi.org/10.1016/1359-835X(96)00064-4

Appendix A. Shear properties for woven composites

In order to plot stress/strain curve in the shear direction, the stress state of the woven specimens is calculated using an analytical model. In the following description, each woven ply is approximated by the superposition of two layers of unidirectional plies. By these approximation, the stress state in the woven could be studied in the same way as the stress state for an angle ply laminate. The stress along the fibre direction in an angle ply laminate can be calculated from the stress transformation equations giving the relationship between stresses expressed in global coordinates and principal material coordinates for an unidirectional layer ([36])

$$\sigma_x = c^2\sigma_1 + s^2\sigma_2 - cs\,\tau_{12} \quad (A.1)$$

$$\sigma_y = s^2\sigma_1 + c^2\sigma_2 + cs\,\tau_{12} \quad (A.2)$$

$$\tau_{xy} = cs\,\sigma_1 + cs\,\sigma_2 + (c^2 - s^2)\,\tau_{12} \quad (A.3)$$

where c and s are cos(θ) and sin(θ) respectively. When an angle ply laminate is loaded along the Y direction, the $+\theta$ and $-\theta$ layers should respect the following equilibrium condition

$$0 = c^2\sigma_1 + s^2\sigma_2 - cs\,\tau_{12} \quad (A.4)$$

$$\sigma_y = s^2\sigma_1 + c^2\sigma_2 + cs\,\tau_{12} \quad (A.5)$$

From Eq. A.4 and Eq. A.5 using the trigonometric identity $s^2+c^2=1$ one has

$$\sigma_y = \sigma_1 + \sigma_2 \quad (A.6)$$

Finally the stresses in the $+\theta$ layer are function also of the strains in the $-\theta$ layer. The procedure (detailed in [36]), gives

$$\sigma_1 = B\sigma_y \quad (A.7)$$

$$\sigma_2 = (1 - B)\sigma_y \quad (A.8)$$

$$\tau_{12} = \frac{1}{2cs}[B\,(1 - 2\,c^2) + c^2]\,\sigma_y \quad (A.9)$$

where B is a parameter combining material properties (Young moduli in two principal material directions E_1 and E_2 and the Poisson coefficient υ_{12}) and trigonometric identities. For $\theta=45$ one has

$$B = \left[\frac{\frac{E_2}{E_1}\upsilon_{12} + 1}{2\frac{E_2}{E_1}\upsilon_{12} + \frac{E_2}{E_1} + 1} \right] \quad \text{(A.10)}$$

and for $E_1 >> E_2$ (as for $\theta=45$ layer), $B \to 1$. On a sample surface the stress state could be obtained from Eq. A.7 – Eq. A.9 in which the stresses are expressed in principal material coordinates as

$$\sigma = \begin{bmatrix} \sigma_1 \\ \sigma_2 \\ \tau_{12} \end{bmatrix} = \begin{bmatrix} \sigma_y \\ 0 \\ \frac{\sigma_y}{2} \end{bmatrix} \quad \text{(A.11)}$$

The stress state of Eq. A.11 is valid when σ_x and τ_{xy} are zero, consequently, to measure the plane shear modulus G_{12}, a tensile test on a $[45]_6$ woven specimen can be employed. In fact the shear strain γ_{12} is given by transformation of the measured axial (ϵ_y) and transversal (ϵ_x) strains. The strain transformation from the laminate theory gives

$$\gamma_{12} = (\epsilon_x - \epsilon_y) \quad \text{(A.12)}$$

hence

$$G_{12} = \frac{\sigma_y}{2(\epsilon_x - \epsilon_y)} \quad \text{(A.13)}$$

DIC strain data points for the quasi static intermediate tensile load/unload cycles do not allow evaluating material properties in the early stages of traction, hence only the secant shear modulus (G_{12}^{sec}) is used to characterize transversal behaviour.

Appendix A. Woven composite mechanical properties - Finite Element model

In this appendix the segmentation result of matrix, warp and weft tows have been employed to extract the geometrical model from a 3D image. A voxel-like meshing is used to obtain a FE model from segmentation results. The segmentation resolution is decreased by 8 times to reduce the voxel number in the FE model, without any important modification of the tow and resin ratios in the composite at the meso-scale. Further details about the FE model employed in this work are reported in ([36]) and Figure 23. Simulations have been carried out on a unit cell model of the woven composite, the dimensions of the segmented unit cell were 9.8×8.7×1.73 mm^3 giving a FE model

including 206×182×36 (1349712) elements. The tows are supposed orthotropic and the homogenized mechanical properties are calculated using the homogenization equations reported in [37], while the matrix is supposed a homogeneous material.

The Young modulus of the matrix has been identified by inverse analysis of a traction test on the woven unit cell. The linear region of the stress-strain curve has been fit from 0 to 0.1% of longitudinal strain using an elastic modulus of the matrix E_m = 2.5 GPa and a Poisson coefficient ν_m = 0.3.

In default of more information on the resin mechanical response, the FE model is the only way to have a Young modulus for the resin to use as input for the homogenised property calculation step for the analytical model presented in Section 5. FE values presented in this paragraph represent the initial values for the elastic longitudinal modulus and stabilized values for the shear secant modulus issued by the experimental activity. A comparison between experimental, numerical and analytical specimen properties is proposed in Appendix B.

The unit cell model has been used to extract the stiffness matrix of the woven specimens along the fibre direction. The numerical homogenization of the elastic properties (Young and shear moduli and Poisson coefficient) has been implemented using periodic boundary condition (PBC) constrains. The "classical" form for the displacement on the boundary surface using PBC equations is in Eq. B.1

$$u_i^{k+} - u_i^{k-} = \epsilon_{ij}^0 (x_j^{k+} - x_j^{k-}) \tag{A.1}$$

where indices k^+ and k^- identify the k^{th} pair of two opposite parallel boundary surfaces of the FE model, ε^0_{ij} is the global (average) strain tensor, x_j are the Cartesian coordinates of a material point and u_i are the displacements, finally i and j are the index 1, 2 and 3 corresponding to the directions X, Y and Z. Applying 6 different values for ε^0_{ij} (3 for pure normal and 3 for pure shear strains), 6 average stresses are obtained. From the applied strain and the resulting average stresses, the complete stiffness matrix C for the $[0]_6$ woven unit cell is obtained.

$$C = \begin{bmatrix} 68.7 & 3.1 & 3.5 & 0 & 0 & 0 \\ 3.1 & 57.8 & 3.4 & 0 & 0 & 0 \\ 3.5 & 3.4 & 9 & 0 & 0 & 0 \\ 0 & 0 & 0 & 3.7 & 0 & 0 \\ 0 & 0 & 0 & 0 & 2.9 & 0 \\ 0 & 0 & 0 & 0 & 0 & 2.9 \end{bmatrix} \text{GPa} \tag{A.2}$$

The terms corresponding to the normal shear strain coupling are quite small compared to the other coefficients. Assuming the orthotropic conditions and plane stress state, the reduced stiffness matrix for the 45° woven allows calculating the material mechanical properties.

Appendix B. Semi-ply based analytical model - Ply mechanical properties

The mechanical properties for the virtual unidirectional ply are calculated using the homogenization equations reported in [37]. The fibre and the matrix are considered isotropic and the fibre

mechanical properties are taken from supplier official datasheet. Fibre thermal properties are issued from ([38], while for the matrix, the thermal expansion coefficient are taken from ([22]). ~~Moreover the Poisson coefficient and the Young modulus for the matrix, the values obtained by the FE model presented in Appendix A are used~~. The phases properties at the test temperature (T=250°C) are resumed in Table 6.

For the unidirectional ply stiffness matrix, the assumptions reported in ([37]) are employed: the unidirectional ply is considered as an orthotropic lamina having negligible out-of-plane stress components. Using the plane stress approximation, the reduced stiffness matrix for the orthotropic lamina is where the index 1 and 2 are referred to the material coordinates illustrated in Figure 25.

$$\overline{Q} = \begin{bmatrix} \overline{Q}_{11} & \overline{Q}_{12} & \overline{Q}_{16} \\ \overline{Q}_{12} & \overline{Q}_{22} & \overline{Q}_{26} \\ \overline{Q}_{16} & \overline{Q}_{26} & \overline{Q}_{66} \end{bmatrix} \tag{B.1}$$

that in the principal material coordinates is reduced to **Q**

$$Q = \begin{bmatrix} Q_{11} & Q_{12} & 0 \\ Q_{12} & Q_{22} & 0 \\ 0 & 0 & Q_{66} \end{bmatrix} \tag{B.2}$$

the coefficients Q_{ij} are calculated starting from the engineering constants issued from the homogenization equations

$$Q_{11} = \frac{E_1}{1 - \nu_{12}\nu_{21}} \tag{B.3}$$

$$Q_{22} = \frac{E_2}{1 - \nu_{12}\nu_{21}} \tag{B.4}$$

$$Q_{12} = \frac{\nu_{21}E_1}{1 - \nu_{12}\nu_{21}} = \frac{\nu_{12}E_2}{1 - \nu_{12}\nu_{21}} \tag{B.5}$$

$$Q_{66} = G_{12} \tag{B.6}$$

where

$$\frac{E_2}{\nu_{21}} = \frac{E_1}{\nu_{12}} \tag{B.7}$$

The woven ply stiffness is then obtained by virtual superposition of 0° and 90° plies as for an angle-ply, neglecting the weaving region of the real woven ply. Considering the warp and weft tow fraction (n_0 and n_{90} respectively) in the composite obtained by μCT scan segmentation, the ply stiffness matrix $\mathbf{Q}_P$ could be calculated as

$$Q_P = n_0 Q_{UD}^0 + n_{90} Q_{UD}^{90} \tag{B.8}$$

The stiffness matrix for the woven ply having the fibre oriented in the 45° direction, named $Q_P^{\pm 45}$, is calculated using the rotation matrix T_1 and T_2

$$T_1 = \begin{bmatrix} c^2 & s^2 & 2cs \\ s^2 & c^2 & -2cs \\ -cs & cs & c^2 - s^2 \end{bmatrix} \tag{B.9}$$

$$T_2 = \begin{bmatrix} c^2 & s^2 & -cs \\ s^2 & c^2 & cs \\ 2cs & -2cs & c^2 - s^2 \end{bmatrix} \tag{B.10}$$

$$Q_P^{\pm 45} = T_1^{-1} Q_P T_2 \tag{B.11}$$

with $c=\cos\theta$ and $s=\sin\theta$. The specimen stiffness matrix is finally obtained using the following expression

$$\begin{bmatrix} N \\ M \end{bmatrix} = \begin{bmatrix} A & B \\ B & D \end{bmatrix} \begin{bmatrix} \varepsilon_0 \\ k \end{bmatrix} \tag{B.12}$$

where **N** and **M** are matrix representing the in-plane force per unit length and moment per unit length respectively. **A** is the matrix representing the in-plane stiffness, **B** defines the bending-stretching coupling and **D** is the bending stiffness matrix. Finally, $\boldsymbol{\varepsilon_0}$ represents the mid-plane strains and **k** the laminate curvature. The explicit expression for these terms is reported in ([37]).

In the following analysis each woven ply is considered as a heterogeneous material along the thickness direction, in other words there is no reasons to suppose that a coupling between the in-plane response and the bending response exists. Consequently the **B** matrix is null, as for laminate symmetric about their mid-plane. Moreover in the follow, the **D** matrix will be neglected being null the applied bending moments. ~~Eq. A.13 is employed for the A matrix calculation~~ **A** matrix is calculated as:

$$A_{\pm 45} = \sum_{i=1}^{l} Q_{P\_i}^{\pm 45} \, t_{P\_i} \tag{B.13}$$

In Eq. B.13 t_{P_i} is the thickness of the ith ply, l is the number of woven plies in the specimen and $\mathbf{A}_{\pm 45}$ is the specimen stiffness matrix. The results obtained for E_m = 2.5 GPa and υ_m = 0.3 are reported in Table 7.

In the values in Table 7 the comparison between experimental and analytical founding is made considering the initial elastic longitudinal modulus and the stabilized value of the secant shear modulus, which is the secant shear modulus value after 50k/70k cycles. As could be remarked, the found values for the composite mechanical properties issued from the analytical model, despite the assumptions on the fibre architecture, are quite close to the experimental ones.

List of Tables

Properties	Value
Fiber Density [g/cc]	1.74-1.83
Cured Matrix Density [g/cc]	1.25
Nominal Prepreg Mass [g/m²]	586
Glass Transition Temperature [°C]	325-335
Matrix Volume Ratio	34-38%

Table 1: T650-35/MVK-14 composite properties ([22]).

Parameter	Value
Stress Ratio R	0.1
Max Stress σ_{MAX} [MPa]	75 (~55% ~~σ^{fail}~~ UTS)
Frequency f (Hz)	2
Maximum Cycles to end	10^6
Temperature	250°C

Table 2: Fatigue test parameters.

Test conditions	Number of cycles to failure
2 bar N_2	1925000
Air	1699205
2 bar O_2	330000

Table 3: Number of cycles to failure for different environmental test conditions.

	ε_0	K	m	n
2 bar N_2	0.27	3.59×10^{-9}	5	0.167
Air	0.34	2.18×10^{-9}	5	0.287
2 bar O_2	0.27	3.34×10^{-9}	5	0.278

Table 4: Nutting's parameters for the interpolation of creep data.

	Air	2 bar O_2	Air/2 bar O_2
τ_1	7000 h	1200 h	5.83
τ_2	310 h	50 h	6.2

Table 5: Characteristic times for the description of the time evolution of γ_{MAX} (Eq. 7), at T=250°C.

Phase Properties	T650-35 Fibre	Polyimide matrix
Young modulus, E [MPa]	240000	2500 (FEM)
Poisson ratio, ν	0.2	0.3 (FEM)
Shear modulus, G [MPa]	100000	961 (FEM)
CTE, α [K^{-1}]	-10^{-7}	5×10^{-5}

Table 6: Mechanical and thermal properties for T650-35 carbon fibre and Polyimide resin at 250°.

Experimental		FE model		Analytical model	
E_y^{ch}	G_{12}^{sec}	E_y^{ch}	G_{12}^{sec}	E_y^{ch}	G_{12}^{sec}
13.9	3.8	13.9	4.2	13.7	3.76

Table 7: Experimental, FE model and analytical longitudinal elastic modulus and secant shear modulus of the woven composite [GPa].

List of Figures

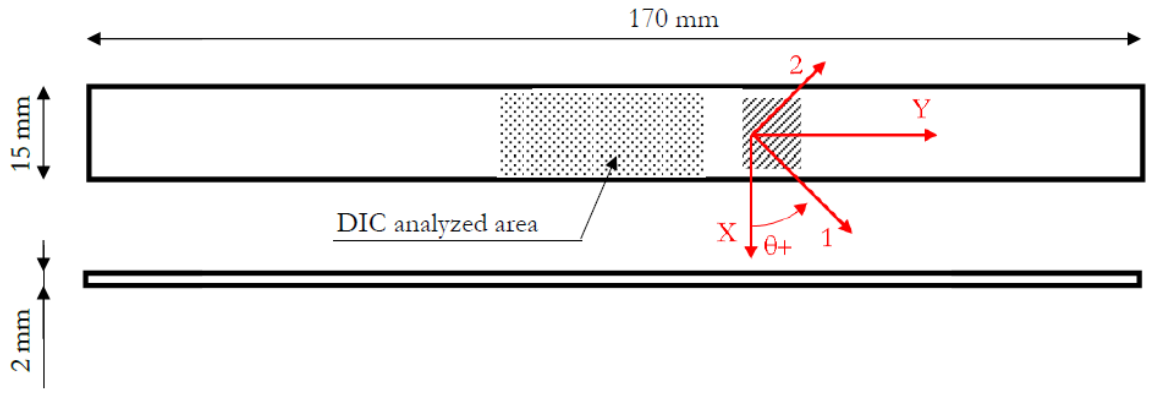

a)

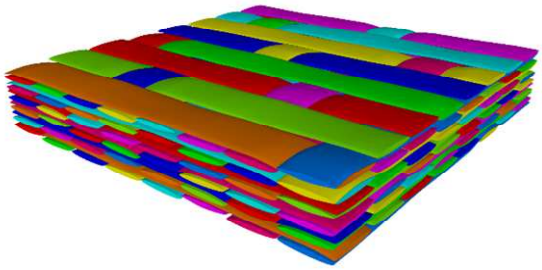

b)

Figure 1: Illustration of samples. **a)** Specimen dimensions and notation used for the woven composite plies. Longitudinal direction is denoted by Y and the transversal one by X, **b)** Schematic representation of ~~8-harness satin (8HS) weave~~ an 8-harness Satin Woven Unit Cell.

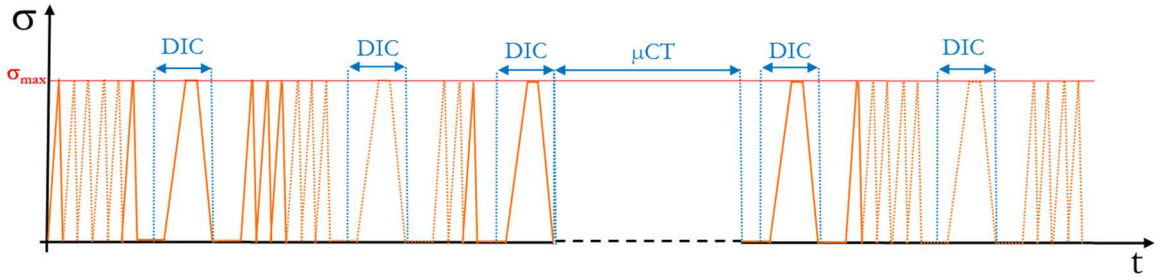

Figure 2: Schematic fatigue test cycle. Fatigue tests are periodically interrupted to perform DIC measures and μCT scans.

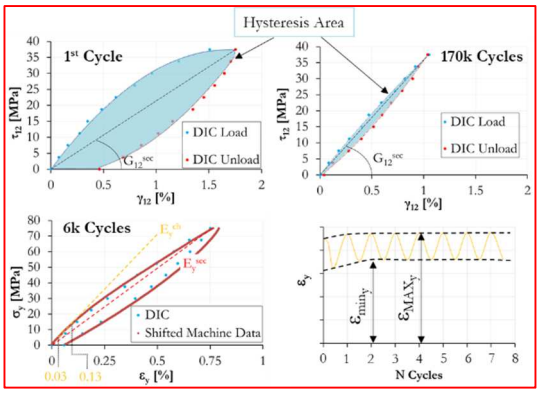

Figure 3: Example of DIC-measured stress-strain curves during fatigue tests, at several cycles. Measured properties extracted from the curves (hysteresis area, elastic longitudinal modulus, and permanent fatigue strain).

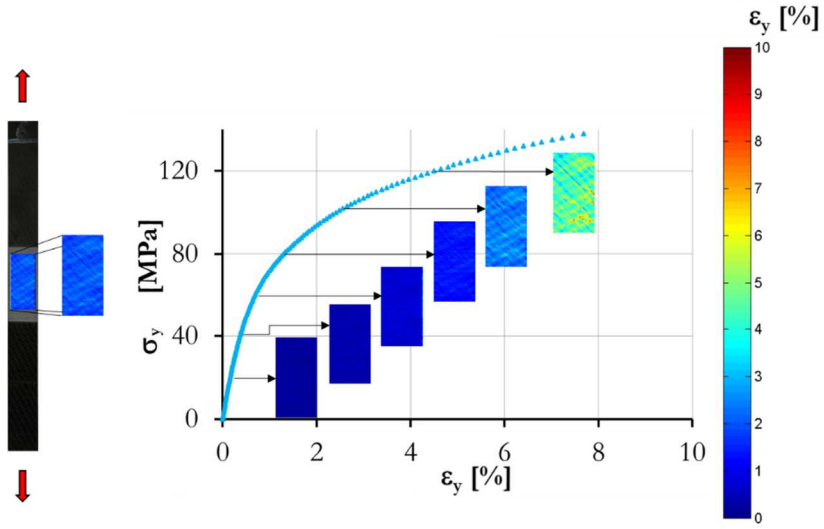

Figure 4: Traction test results 8-harness Satin Woven carbon fibre/polyimide matrix specimen. Stress-strain curve and DIC strain fields during the test.

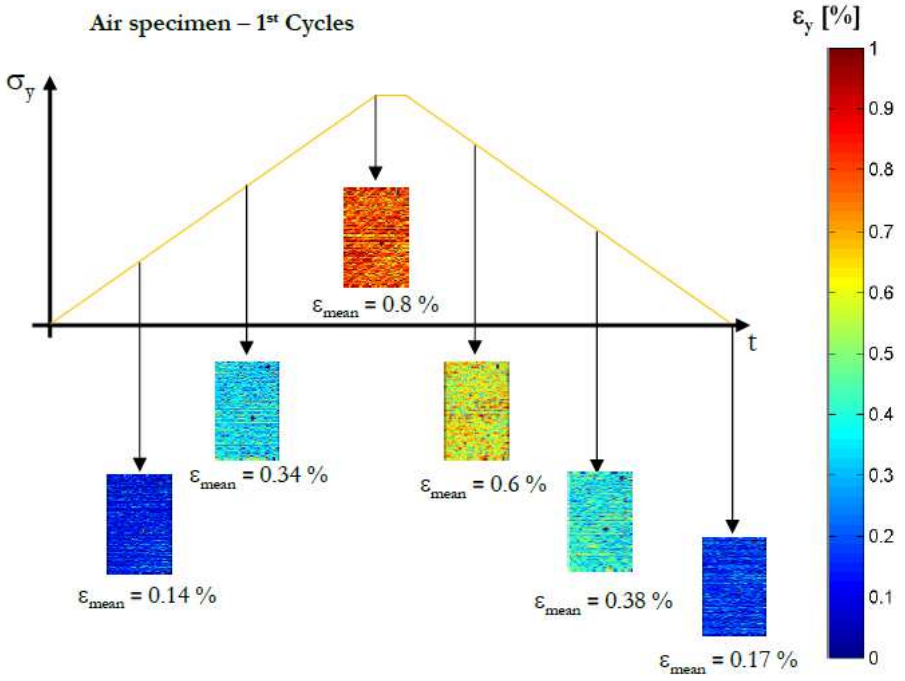

a)

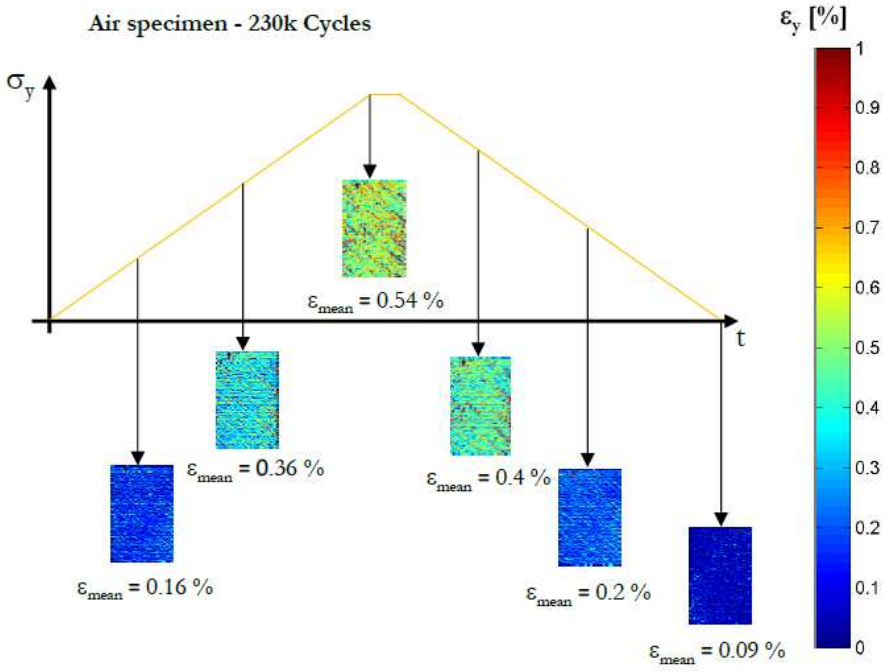

b)

Figure 5: DIC strain fields measured on the specimen surface during a load/unload intermediate stop for the air specimen after **a)** 1 and **b)** 230k cycles.

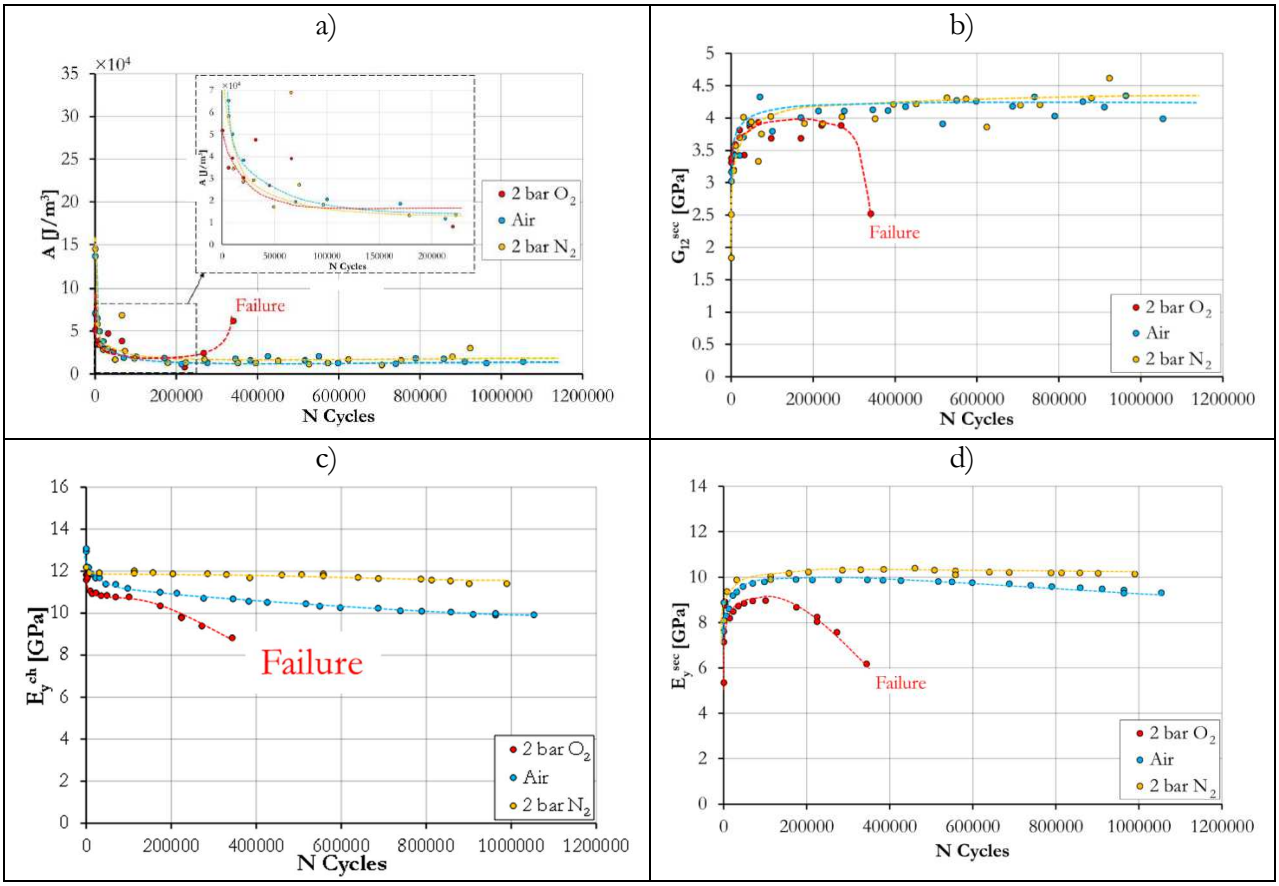

Figure 6: Evolution of **a)** the hysteresis area, A **b)** secant shear modulus, G_{12}^{sec} **c)** chord longitudinal modulus, E_y^{ch} **d)** secant longitudinal modulus, E_y^{sec}, as function of the number of cycle during fatigue tests.

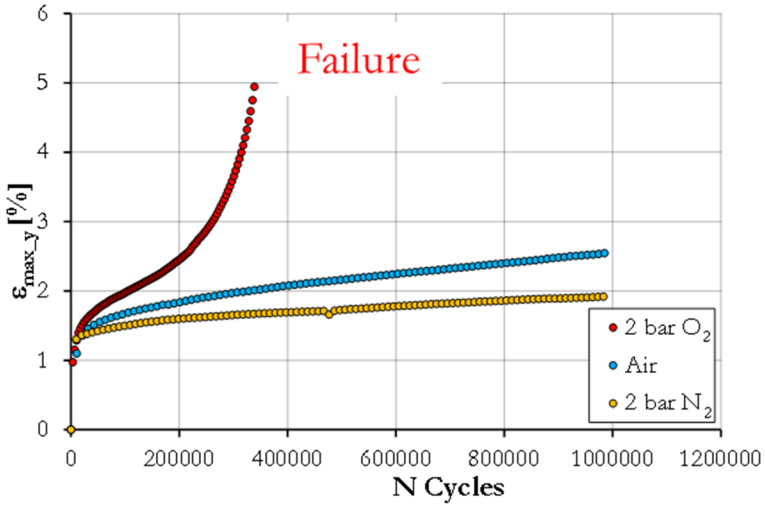

Figure 7: Evolution of the maximal residual strain, ε_{max_y}, as function of the number of cycle during continuous fatigue tests.

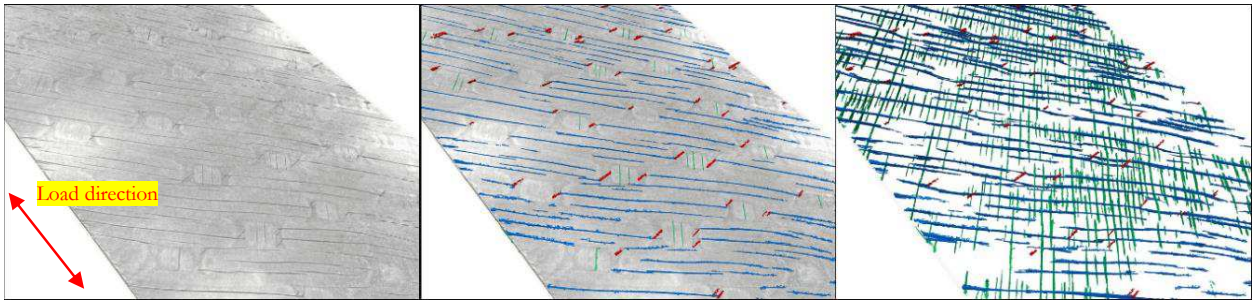

Figure 8: Specimen tested in 2 bar O_2 after 550k cycles: segmentation of an external ply. In the reconstructed image ply, cracks are segmented and the segmentation result is reported in the last image. Red segments are 0° cracks, the blue and green ones are associated to -45° and +45° cracks respectively.

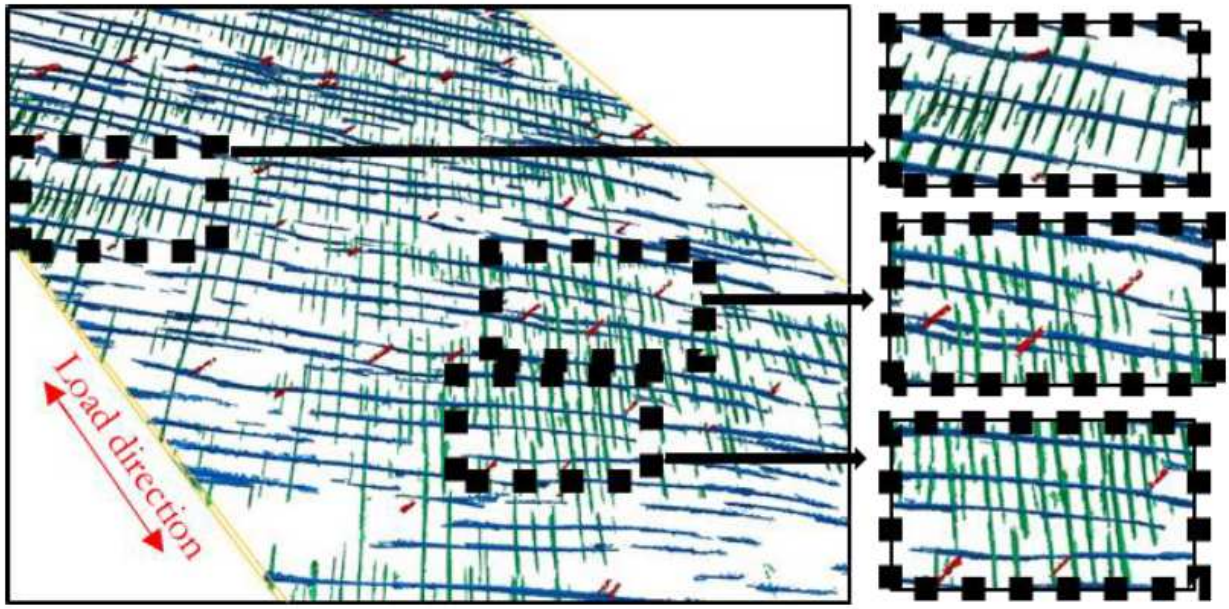

Figure 9: Zoom of the segmentation reported in Figure 8. Detail of the cracks in the 45° direction. Red segments are 0° cracks, the blue and green ones are associated to -45° and +45° cracks respectively.

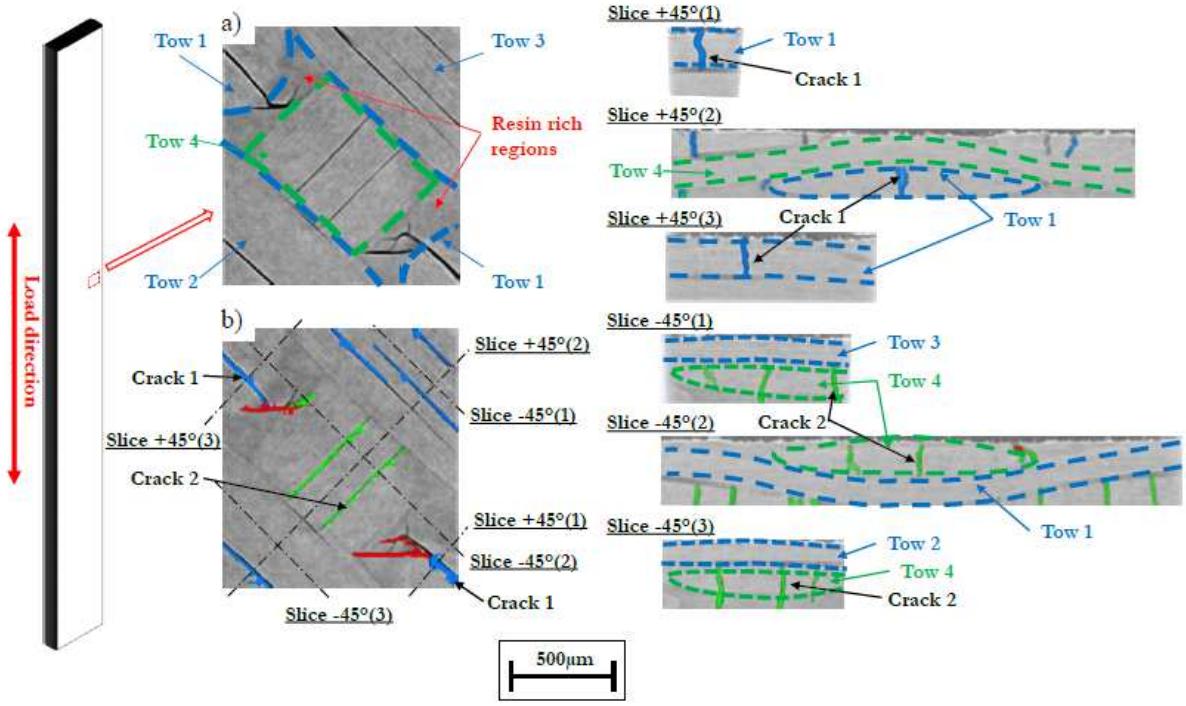

Figure 10: Representative region of the damaged external woven ply in Figure 8. In **a)** the external slice of the ply shows tows in -45° and +45° direction, resin rich regions and cracks. The segmentation results are in **b)** and the whole crack paths are shown using the cutting planes in +45 and -45° direction.

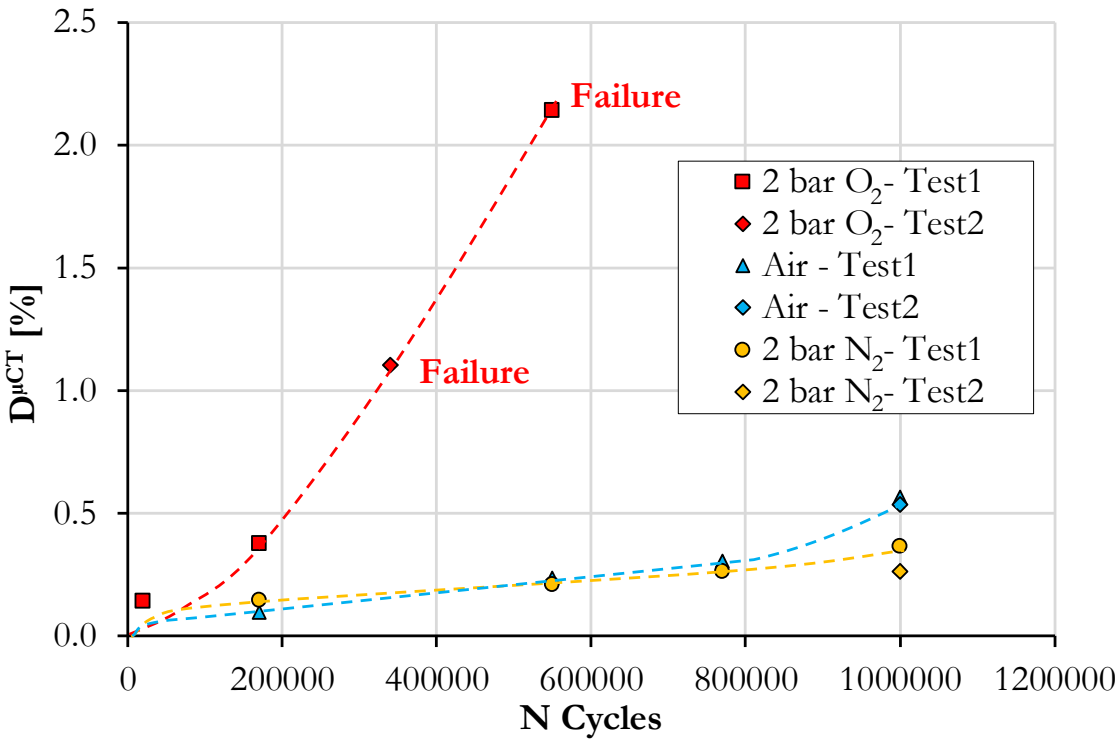

Figure 11: Evolution of the volumetric crack density $D^{\mu CT}$ during fatigue.

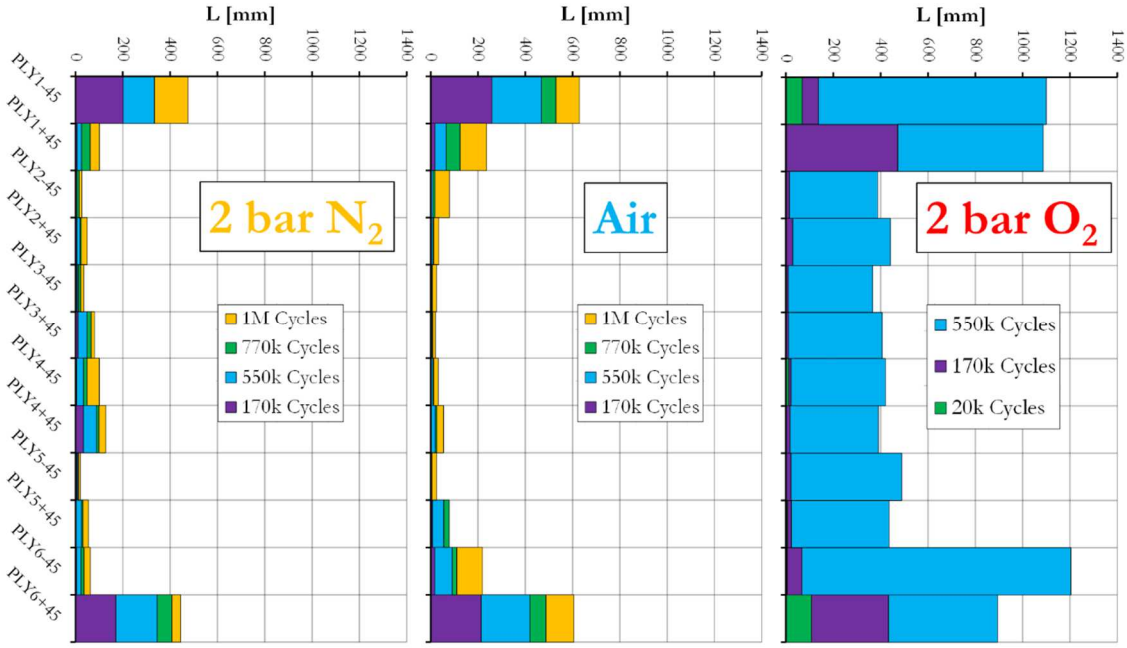

Figure 12: Through the thickness crack distribution for the three environmental test conditions. The vertical axis represents the vertical position of each ply.

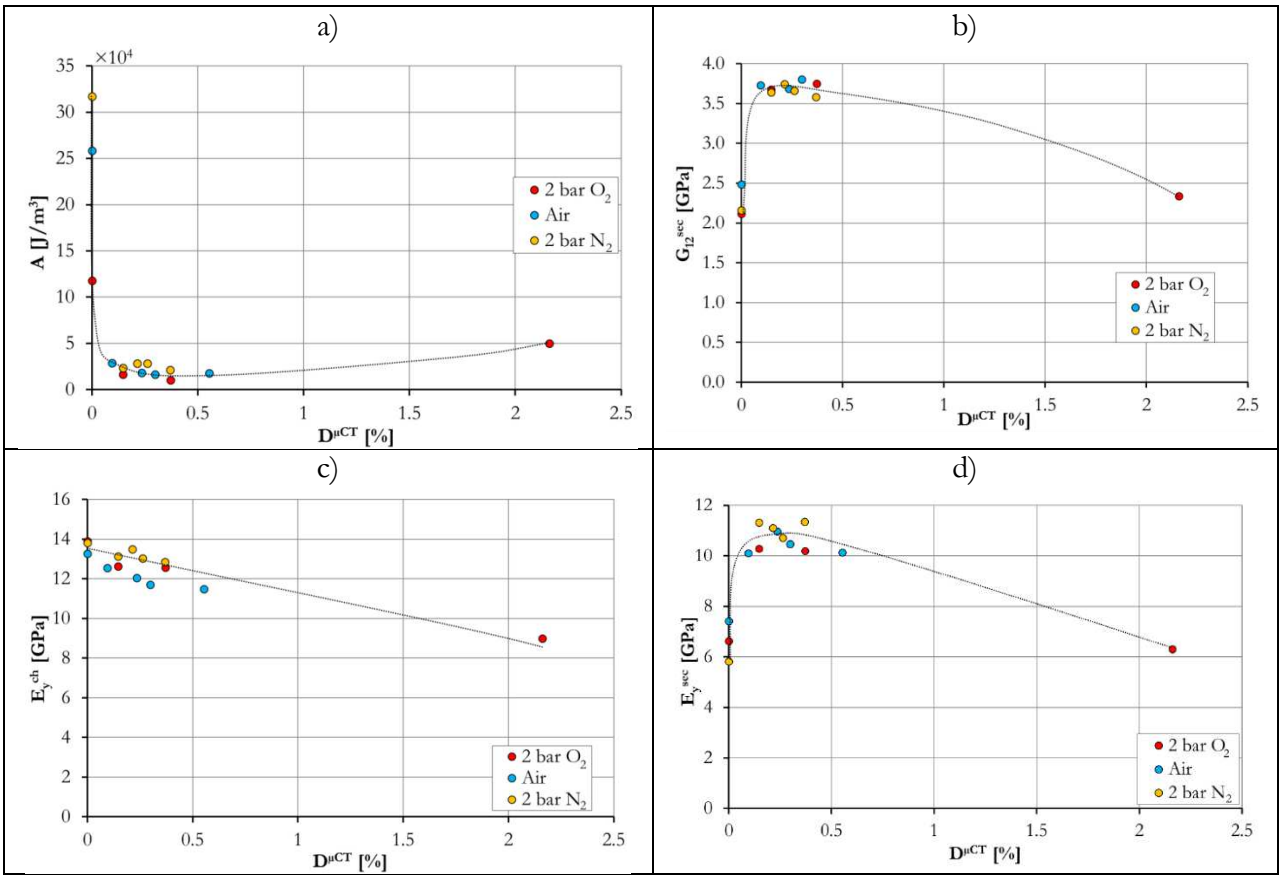

Figure 13: Evolution of **a)** the hysteresis area, A **b)** secant shear modulus, G_{12}^{sec} **c)** chord longitudinal modulus, E_y^{ch} **d)** secant longitudinal modulus, E_y^{sec}, as function of the volumetric crack density, $D^{\mu CT}$, for all tested samples.

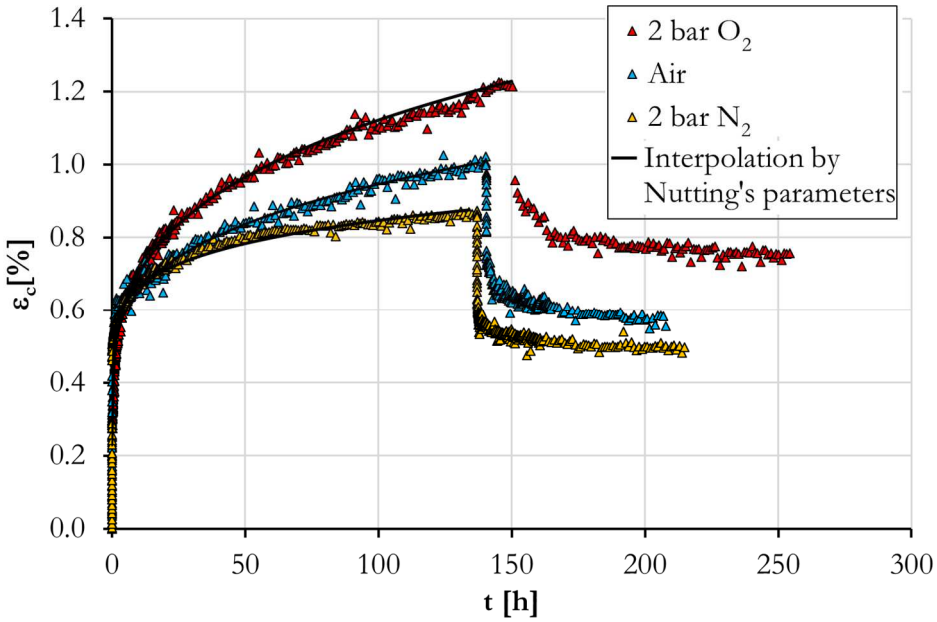

Figure 14: Creep test results and interpolation by using Nutting's parameters.

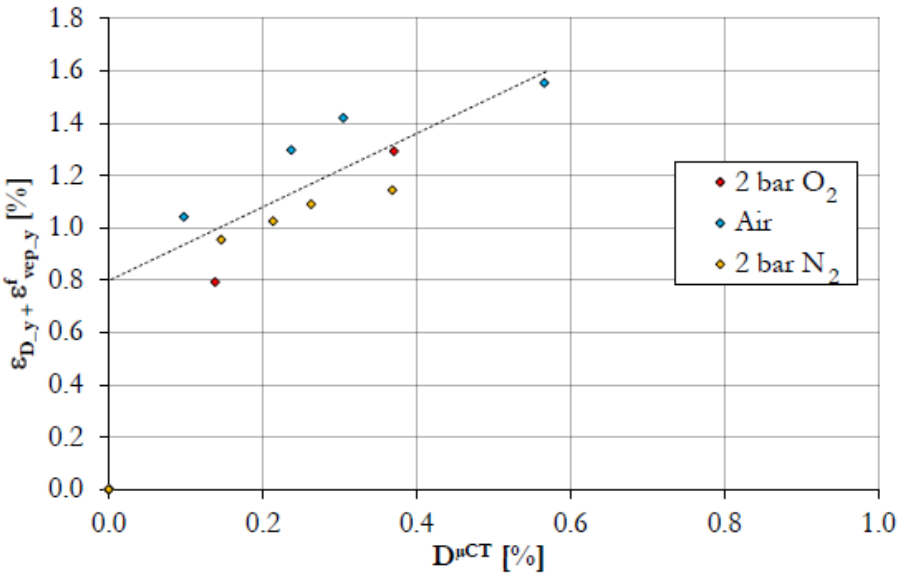

Figure 15: Evolution of the strain $\varepsilon_{D\_y}+\varepsilon_{vep\_y}^{f}$ as a function of the volumetric crack density $D^{\mu CT}$ during fatigue.

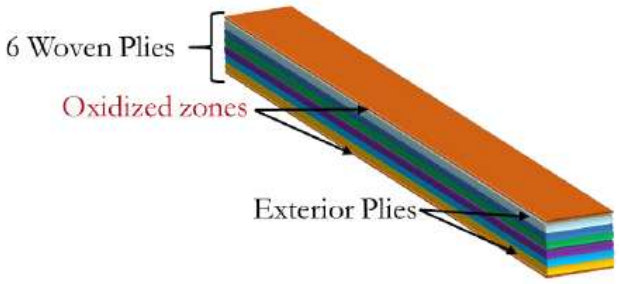

Figure 16: Schematization of a 6 plies woven specimen. The main oxidized regions are located in the external plies.

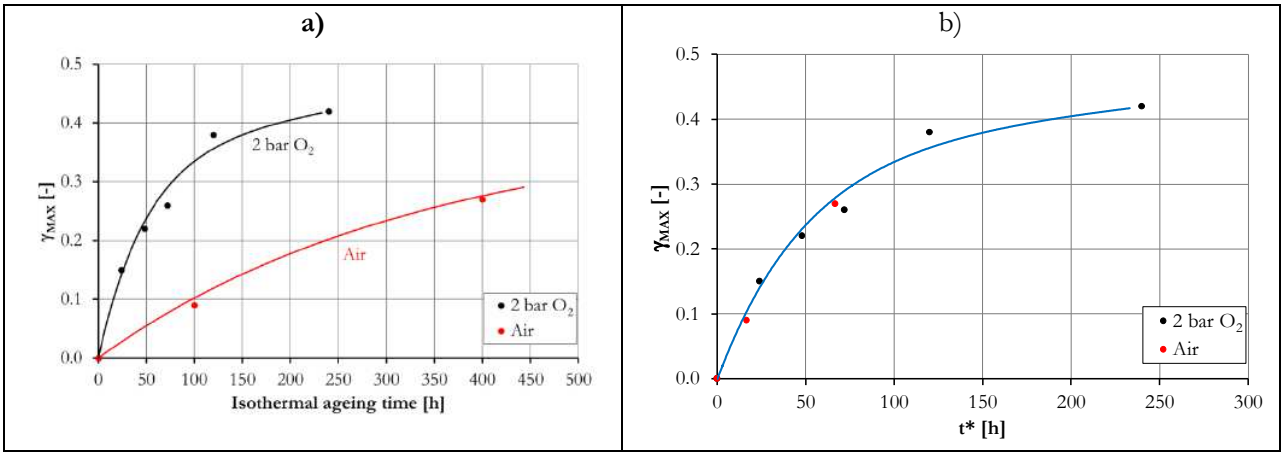

Figure 17: Evolution of the ageing parameter measured at the external surface exposed to the environment (γ_{MAX}) as a function of **a)** the ageing time **b)** the ~~adimensional~~ reduced ageing time in 2 bar O_2 and air at 250°C.

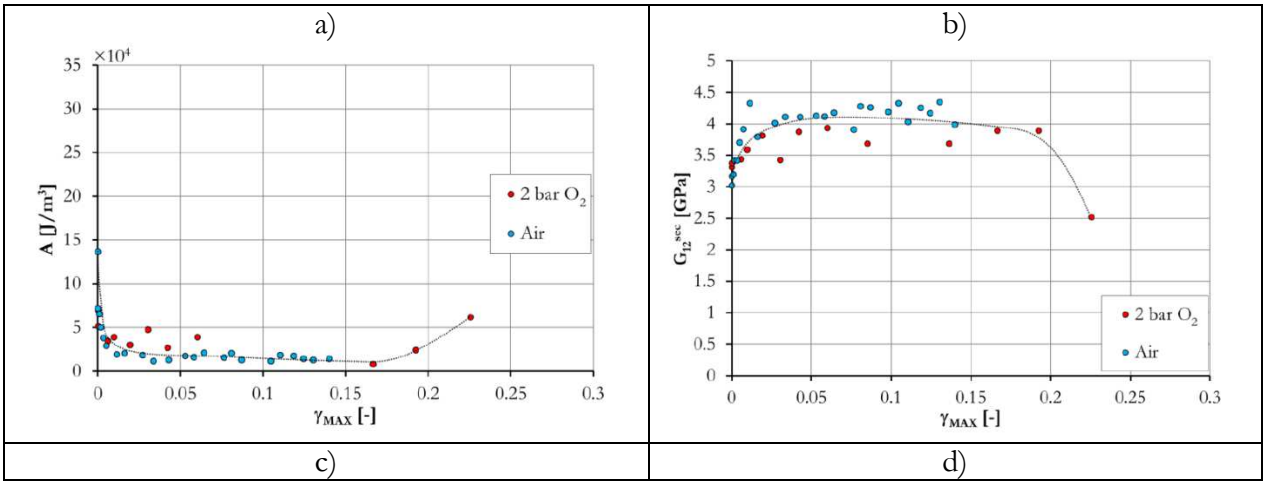

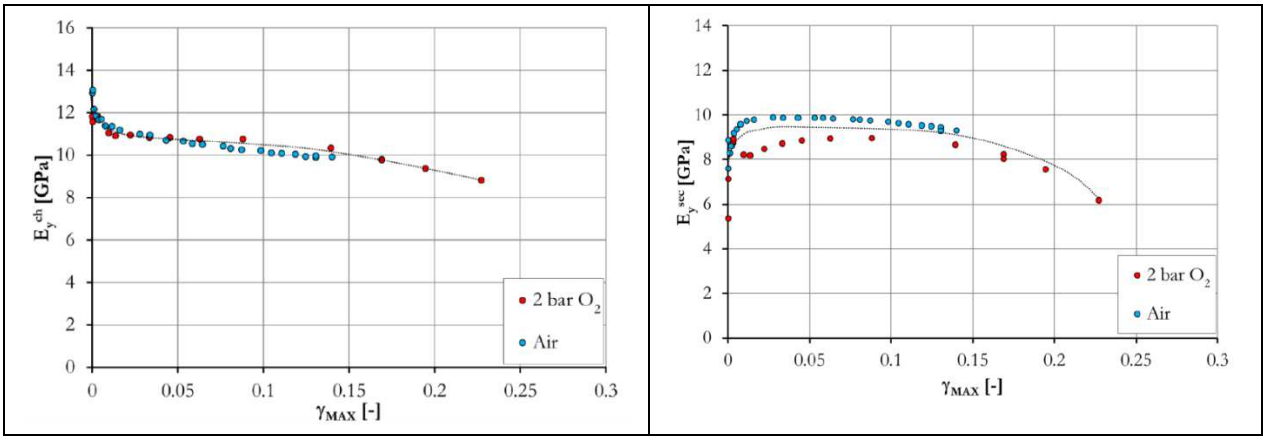

Figure 18: Evolution of **a)** the hysteresis area, A **b)** secant shear modulus, G_{12}^{sec} **c)** chord longitudinal modulus, E_y^{ch} **d)** secant longitudinal modulus, E_y^{sec}, as function of the oxidation tracer, γ_{max}.

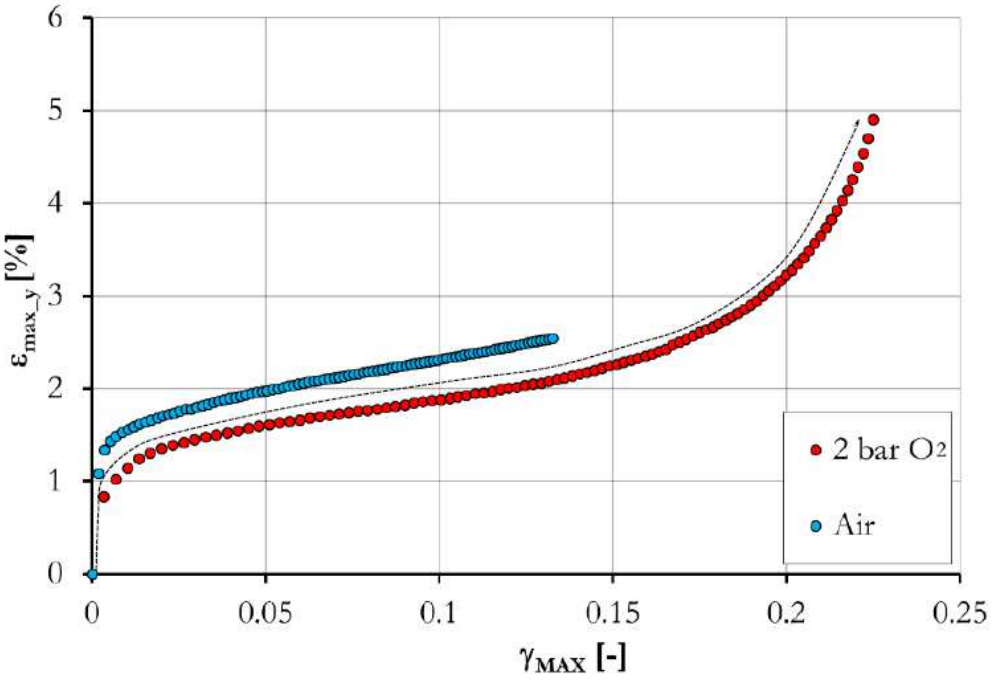

Figure 19: Evolution of ε_{max_y} as function of the oxidation tracer (aging parameter), γ_{max}.

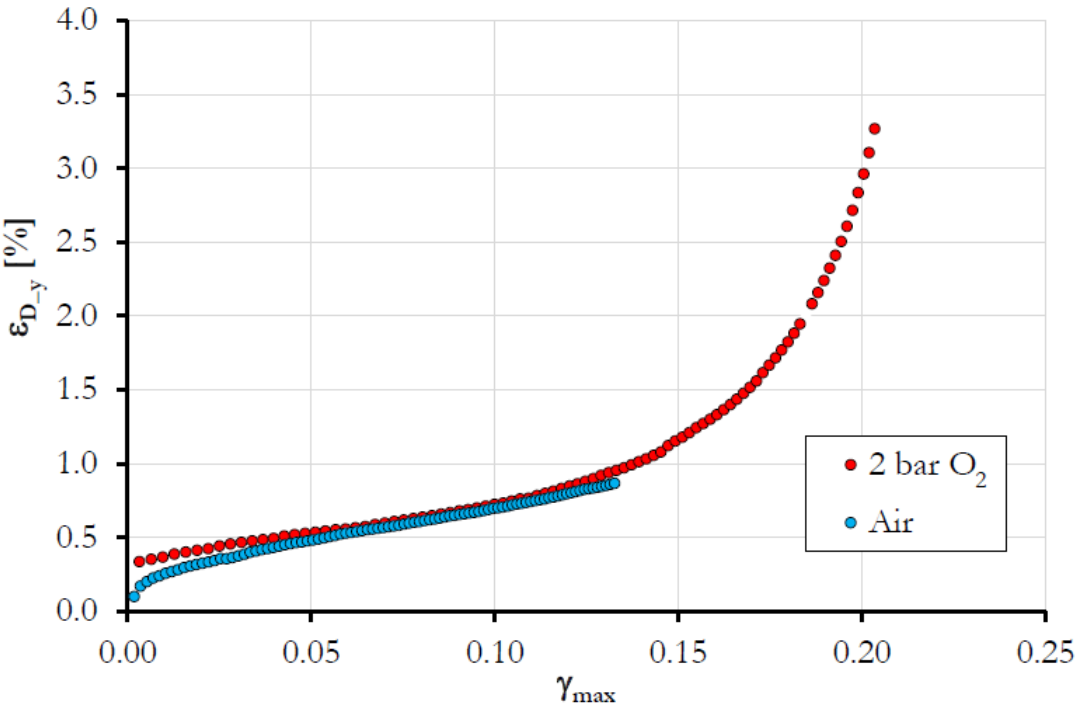

Figure 20: Evolution of ε_{D_y} as function of the oxidation tracer (aging parameter), γ_{max}.

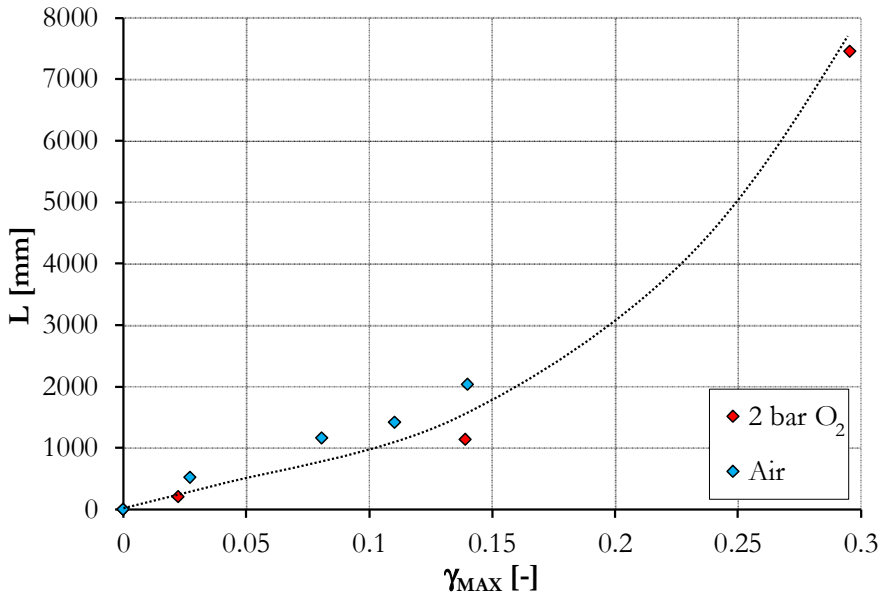

Figure 21: Evolution of L as function of the oxidation tracer (aging parameter), γ_{max}.

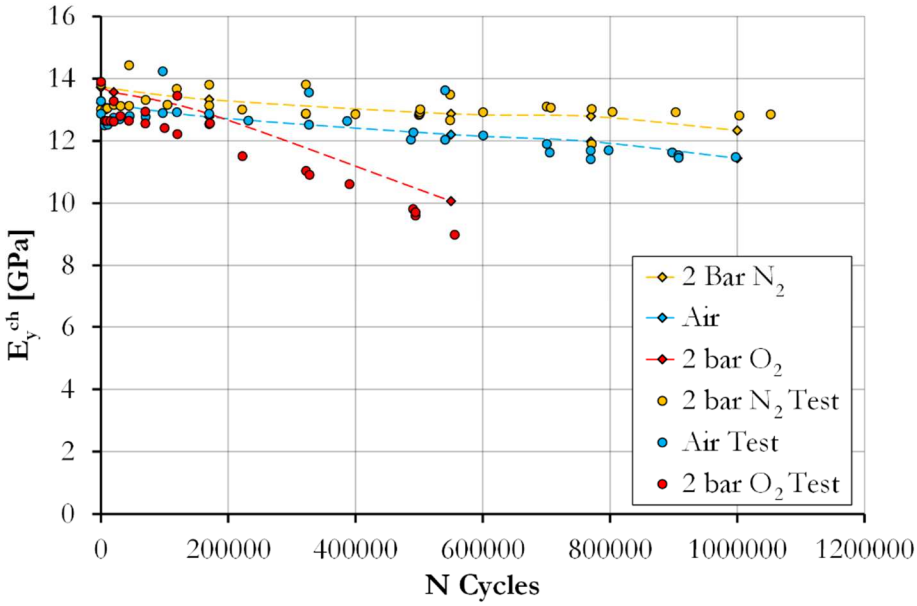

Figure 22: Evolution of the longitudinal chord modulus, E_y^{ch}, during fatigue, with increasing the number of cycles, including the prediction of the analytical model.

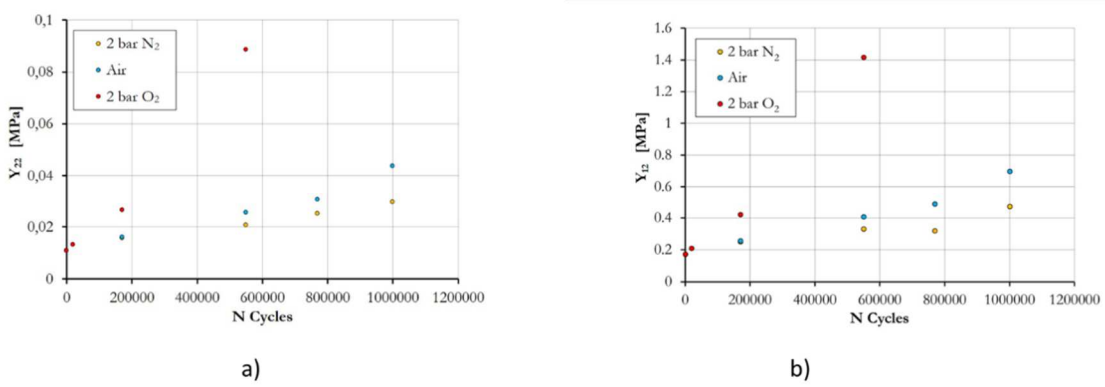

Figure 23: Evolution of the predicted values of the thermodynamics forces, a) Y_{22} and b) Y_{12} in the +45° ply as a function of number of cycles.

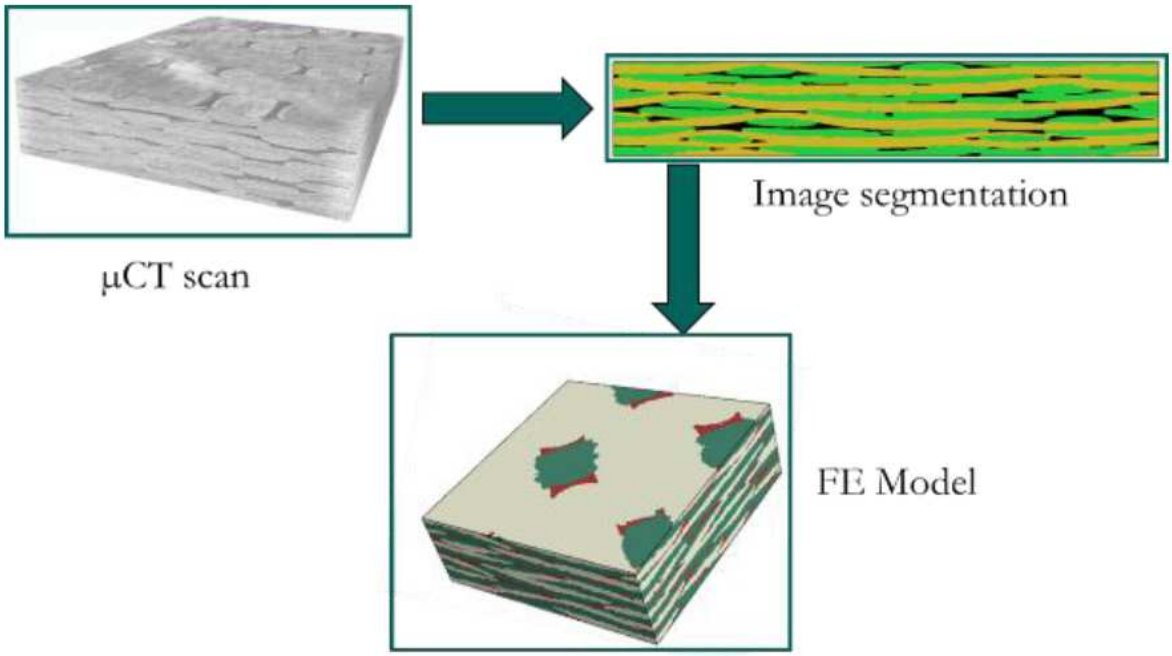

Figure 24: FE model issued by a µCT scan of a composite unit cell. A mesh is directly created using the image segmentation.

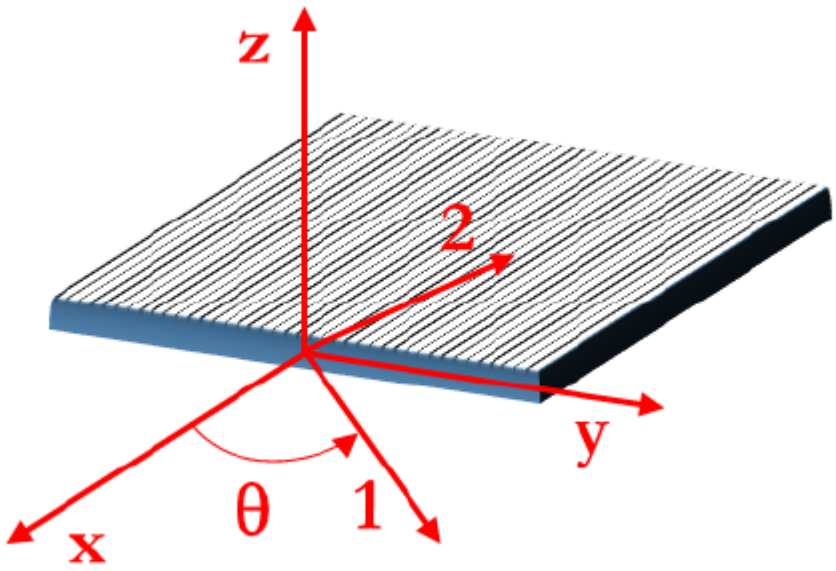

Figure 24: Global and principal material coordinates.